

2

DTIC FILE COPY

TECHNICAL REPORT BRL-TR-3119

BRL

AD-A224 354

SUPersonic/HYPersonic AERODYNAMICS
AND HEAT TRANSFER FOR PROJECTILE DESIGN
USING VISCOUS-INVISCID INTERACTION

DTIC
ELECTE
JUL 25 1990
D^{ay}D

MICHAEL J. NUSCA

JUNE 1990

APPROVED FOR PUBLIC RELEASE; DISTRIBUTION UNLIMITED.

U.S. ARMY LABORATORY COMMAND

BALLISTIC RESEARCH LABORATORY
ABERDEEN PROVING GROUND, MARYLAND

90 07 24 036

NOTICES

Destroy this report when it is no longer needed. DO NOT return it to the originator.

Additional copies of this report may be obtained from the National Technical Information Service, U.S. Department of Commerce, 5285 Port Royal Road, Springfield, VA 22161.

The findings of this report are not to be construed as an official Department of the Army position, unless so designated by other authorized documents.

The use of trade names or manufacturers' names in this report does not constitute indorsement of any commercial product.

UNCLASSIFIED**REPORT DOCUMENTATION PAGE**

Form Approved
OMB No. 0704-0188

Public reporting burden for this collection of information is estimated to average 1 hour per response, including the time for reviewing instructions, searching existing data sources, gathering and maintaining the data needed, and completing and reviewing the collection of information. Send comments regarding this burden estimate or any other aspect of this collection of information, including suggestions for reducing the burden, to Washington Headquarters Service, Directorate for Information Operations and Support, 1215 Jefferson Davis Highway, Suite 1204, Arlington, VA 22202-4162, and to the Office of Management and Budget, Paperwork Reduction Project 0704-0188, Washington, DC 20503.

1. AGENCY USE ONLY (Leave blank)	2. REPORT DATE	3. REPORT TYPE AND DATES COVERED
	June 1990	Final May 89 - May 90
4. TITLE AND SUBTITLE	5. FUNDING NUMBERS	
Supersonic/Hypersonic Aerodynamics and Heat Transfer for Projectile Design Using Viscous-Inviscid Interaction	1L162618AHB0	
6. AUTHOR(S)	7. PERFORMING ORGANIZATION NAME(S) AND ADDRESS(ES)	
Michael J. Nusca	8. PERFORMING ORGANIZATION REPORT NUMBER	
9. SPONSORING / MONITORING AGENCY NAME(S) AND ADDRESS(ES)	10. SPONSORING / MONITORING AGENCY REPORT NUMBER	
Ballistic Research Laboratory ATTN: SLCBR-DD-T Aberdeen Proving Ground, MD 21005-5066	BRL-TR-3119	
11. SUPPLEMENTARY NOTES		
12a. DISTRIBUTION / AVAILABILITY STATEMENT		12b. DISTRIBUTION CODE
Approved for public release; distribution is unlimited.		
13. ABSTRACT (Maximum 200 words)		
<p>An aerodynamic design code for axisymmetric projectiles has been developed using a viscous-inviscid interaction scheme. Separate solution procedures for inviscid (Euler) and viscous (boundary layer) flowfields are coupled by an iterative solution procedure. This code yields body surface flow profiles in less than one minute of run time on minicomputers. These surface profiles represent converged solutions to both the inviscid and viscous equations. The capability of computing local reverse flow regions is included. The procedure is formulated for supersonic and hypersonic Mach numbers including both laminar and turbulent flow. In addition, aerodynamic heating equations are used to compute heat transfer coefficient and local Stanton number from flow profiles. Computed surface pressure profiles for Mach numbers 2 thru 5 and 8 and computed aerodynamic stability for Mach numbers 3 thru 6 are compared to wind tunnel measurements on cone-cylinder-flare projectiles. Computed surface heat transfer coefficients are compared to results obtained from wind tunnel measurements on cone-cylinder-flare, flat plate, and blunt-cone models at Mach numbers 5 and 10.</p>		
14. SUBJECT TERMS		
<p>Hypersonic Flow; Computational Aerodynamics; Boundary Layers;</p>		
<p>Heat Transfer; Projectile Design</p>		
15. NUMBER OF PAGES		
62		
16. ACCESSION CODE		
17. SECURITY CLASSIFICATION OF REPORT	18. SECURITY CLASSIFICATION OF THIS PAGE	19. SECURITY CLASSIFICATION OF ABSTRACT
UNCLASSIFIED	UNCLASSIFIED	UNCLASSIFIED
20. LIMITATION OF ABSTRACT		
SAR		

Table of Contents

	<u>Page</u>
List of Figures	v
List of Tables	vii
I. INTRODUCTION	1
II. BACKGROUND	2
III. INTERACTION MODEL	6
1. Inviscid Methods	6
a. Linearized Perturbation Theory	6
b. Second-Order Shock-Expansion Theory	9
c. Cone Surface Pressure	12
d. Modified-Newtonian Theory	13
2. Viscous Methods	13
a. Standard Solution Procedure	16
b. Inverse Solution Procedure	17
3. Interaction Method	19
4. Small Yaw Procedure	20
IV. HEAT TRANSFER ANALYSIS	21
V. CODE VALIDATION	24
1. Flow Profiles	24
2. Aerodynamic Stability	26
3. Heat Transfer Profiles	28
VI. CONCLUSIONS	30
REFERENCES	33
LIST OF SYMBOLS	55
DISTRIBUTION LIST	59

INTENTIONALLY LEFT BLANK.

List of Figures

<u>Figure</u>	<u>Page</u>
1 Linearized Perturbation Theory - Maximum Body Angle vs. Mach Number	39
2 Oblique Shock Theory - Maximum Body Angle vs. Mach Number	40
3 Variation of $(C_p)_{cone}/(C_p)_{wedge}$ with $\text{LOG}_{10}(M_\infty \delta^\circ)$	41
4 Wind Tunnel Data (C_p) vs. Inviscid Flow ($\text{Re} = \infty$) and INTERACT; 4° Flare, Mach = 2	42
5 Comparison of Wind Tunnel Data (C_p) with INTERACT Results; 4° Flare, Mach = 2,4	43
6 Comparison of Wind Tunnel Data (C_p) with INTERACT Results; 6° Flare, Mach = 2,4,5	44
7 Comparison of Wind Tunnel Data (C_p) with INTERACT Results; 8° Flare, Mach = 2,4,5	45
8 Comparison of Wind Tunnel Data (C_p) with INTERACT Results; 20° Flare, Mach = 3,8,1	46
9 Comparison of Wind Tunnel Data (C_p) with INTERACT Results; 6° Flare, Mach = 2, $\alpha = 1^\circ$	47
10 Comparison of Wind Tunnel Data (\dot{q}_w) with INTERACT Results; Flat Plate, Mach = 10.53	48
11 Comparison of Wind Tunnel Data (\dot{q}_w) with INTERACT Results; Blunt Cone, Mach = 10.6	49
12 Comparison of Wind Tunnel Data (\dot{q}_w) with INTERACT Results; 5° Flare, Mach = 5.2	50
13 Comparison of Wind Tunnel Data (\dot{q}_w) with INTERACT Results; 5° Flare, Mach = 5.2, $\alpha = 0^\circ$ and 1.25°	51
14 Comparison of Wind Tunnel Data (\dot{q}_w) with INTERACT Results; 5° Flare, Mach = 5.2, $\alpha = 1.25^\circ$	52
15 Comparison of Wind Tunnel Data (\dot{q}_w) with INTERACT Results; 10° Flare, Mach = 5.2, $\alpha = 0^\circ$ and 1.25°	53
16 Comparison of Wind Tunnel Data (\dot{q}_w) with INTERACT Results; 10° Flare, Mach = 4.98	54

INTENTIONALLY LEFT BLANK.

List of Tables

<u>Table</u>		<u>Page</u>
1	AERODYNAMIC DESIGN CODES FOR AXISYMMETRIC BODIES . . .	5
2	VARIATION OF CENTER OF PRESSURE WITH MACH NUMBER . . .	27
3	EFFECT OF REYNOLDS NUMBER ON FLARE HEAT TRANSFER . .	30

Accession For	
NTIS	CRA&I <input checked="" type="checkbox"/>
DTIC	TAB <input type="checkbox"/>
Unannounced <input type="checkbox"/>	
Justification _____	
By _____	
Distribution / _____	
Availability Codes	
Dist	Avail and / or Special
A-1	



INTENTIONALLY LEFT BLANK.

I. INTRODUCTION

Armor-piercing, fin-stabilized, sabot-discarding (APFSDS) kinetic energy projectile configurations consist of long rod cone-cylinder bodies with a set of tail fins to provide aerodynamic stability. An alternate design consists of a flared afterbody as the stabilizing element. The flared projectile design has been investigated for training round applications.¹⁻³ Recently, interest has been generated in extending the flight Mach number for APFSDS projectiles as high as 8.0. Investigations of electro-magnetic (EM)⁴ and electro-thermal (ET)⁵ gun propulsion systems as well as ramaccelerator (or in-bore ramjet) gun systems⁶ have shown that the projectile muzzle velocity could reach 3 km/s. These projectiles generally fly low altitude trajectories at small angles of yaw. Under these conditions the effects of aerodynamic heating and thermal damage to the projectile become critical design issues. The need for computationally rapid projectile design codes that can accurately predict aerodynamic drag and moment coefficients as well as surface heat transfer, is apparent. These codes form the initial stage of a design cycle that also includes real-gas (equilibrium-air or reacting-flow) Navier-Stokes fluid dynamics codes that are computationally expensive.

Preliminary design and evaluation of proposed projectile configurations require rapid, reasonably accurate methods to predict aerodynamic characteristics. Two different approaches have predominantly been employed to calculate aerodynamic coefficients using predictive methods: computational fluid dynamics (CFD) using numerical techniques to solve the full Navier-Stokes equations and rapid engineering approximate codes using semi-empirical and analytical methods. The first approach is more generalized and can accept a wide variety of freestream conditions and body geometries. In principle, the results obtained are more accurate than those obtained using the second approach; however, CFD methods require considerable computational time and cost, and their accuracy depends on selected numerical grid sizes. These difficulties have restricted CFD applications from engineering problems where rapid design tools are required. Instead, CFD serves as a followup to engineering design codes, where the latter is used to rapidly narrow the field of viable projectile design candidates while the former is used to finalized the design and assess the aerodynamic impact of fine geometric changes.

Engineering design codes employ approximate linear analyses as well as experimental data. Most of the classical techniques have been proven over the years to be accurate aerodynamic predictive methods. However, a considerable amount of research is still needed to improve and extend these predictive tools. In general, the areas of necessary improvement

¹ Celmins, I., "Drag and Stability Tradeoffs for Flare-Stabilized Projectiles," U.S. Army Ballistic Research Laboratory, Aberdeen Proving Ground, MD., report in preparation.

² Celmins, I., "Aerodynamic Characteristics of Fin- and Flare-Stabilized 25mm XM910 Prototypes," BRL-TR-2882, U.S. Army Ballistic Research Laboratory, Aberdeen Proving Ground, MD., Dec. 1987.

³ Mermagen, W.H., and Yalamanchili, R.J., "The Effect of Perforations on the Ballistics of a Flare-Stabilized Projectile," AIAA-86-2024, Proceedings of the 13th AIAA Atmospheric Flight Mechanics Conference, Williamsburg VA, August 18-20, 1986.

⁴ Garner, J.M., Zielinski, A.E., and Jamison, K.A., "Design and Testing of a Mass-Stabilized Projectile for a Small Caliber Electromagnetic Gun," BRL-MR-3744, U.S. Army Ballistic Research Laboratory, Aberdeen Proving Ground, MD, April 1989.

⁵ Pengelley, R., and Sweetman, B., "FMC's CAP (Combustion Augmented Plasma) Gun," International Defense Review, July 1989, pp. 813-815.

⁶ Hertzberg, A., Bruckner, A.P., and Bogdenoff, D.W., "Ram Accelerator: A New Chemical Method for Accelerating Projectiles to Ultrahigh Velocities," AIAA Journal, Vol. 26, No. 2, February 1988, pp. 195-203.

include extended scope of applicability, ease of usage, and code robustness.

This report examines an engineering design code, INTERACT, written at the U.S. Army Ballistic Research Laboratory,⁷ that employs a viscous-inviscid interaction procedure for evaluation of axisymmetric projectiles. Separate solution methods for inviscid (Euler) and viscous (boundary layer) flowfields are coupled by an interaction model that includes an iterative solution procedure. Inviscid methods include: linearized perturbation theory, second-order shock-expansion theory, modified-Newtonian theory, and combinations of these theories for certain sections of the projectile geometry. The viscous method employed is a finite-difference, second-order, Keller-Box scheme for standard and inverse solutions of the boundary-layer equations. INTERACT yields body surface flow profiles and boundary layer profiles in less than one minute of run time on minicomputers. These surface profiles represent converged solutions to both the inviscid and viscous equations rather than an inviscid solution updated by the presence of the boundary layer. The capability of computing local reverse flow regions is included. The procedure is formulated for supersonic and hypersonic Mach numbers including both laminar and turbulent flow Reynolds numbers. Real-gas and high temperature effects are not included in the aerodynamic analysis. Approximate methods for aerodynamic heat transfer analysis, assuming gas at chemical equilibrium, have been included. The heat transfer equations use body surface flow distributions and compute the surface heat transfer coefficient and local Stanton number.

Computations of surface pressure profiles for Mach numbers 2 thru 5 and 8 are compared to wind tunnel measurements on cone-cylinder-flare projectiles. Computations of aerodynamic stability (center of pressure) for Mach numbers 3 thru 6 are compared to wind tunnel measurements on a cone-cylinder-flare projectile. Computations for surface heat transfer coefficient are compared to results obtained from wind tunnel measurements on cone-cylinder-flare, flat plate, and blunt-cone models at Mach numbers 5 and 10.

II. BACKGROUND

In recent years engineering design codes have been constructed for the rapid prediction of aerodynamic coefficients. Two classes of codes have emerged: semi-empirical methods and component build-up methods. The code derived in this report addresses a third class; viscous-inviscid interaction methods. Some of the available codes are described below and summarized in Table 1.

Semi-empirical codes are formulated from a database of experimental and test data spanning certain ranges of Mach and Reynolds numbers and for certain projectile configurations. A specific code is usually limited to either spin-stabilized, small L/D projectiles or non-spinning, fin- or flare-stabilized long-rod configurations. Limitations on the accuracy and/or applicability of the code occur whenever the flight conditions and/or projectile geometry exceed the range of the database. Examples of semi-empirical codes for spin-stabilized projectiles consisting of a conical or ogival nose section, cylinder mid-section, and

⁷Nesca, M.J., "Computational Aerodynamics for Axisymmetric Cone-Cylinder-Flare Projectiles in Supersonic Flight," AIAA-85-1657, Proceedings of the 12th AIAA Atmospheric Flight Mechanics Conference, Snowmass CO, August 19-21, 1985.

boattail or flared afterbody include: McDAG,⁸ Donovan and Wood,⁹ Donovan,¹⁰ and Morris.¹¹ For fin- and flare-stabilized long-rod projectiles the codes include: Donovan, Nusca, and Wood,¹² Donovan and Grollman,¹³ and Donovan.¹⁴ The PRODAS code by Whyte et.al.¹⁵⁻¹⁷ is formulated to predict the aerodynamics of both spin- and fin-stabilized projectiles and includes interior, exterior, and terminal ballistics modules.

Component build-up codes are formulated using classical theories for the prediction of linear aerodynamics, and semi-empirical formulae for special cases (e.g. high angle of attack, turbulent flow). In these schemes, various theories or semi-empirical formulae are applied to isolated sections of the projectile configuration and then combined with predicted interference effects to yield the overall aerodynamic coefficients. While these codes are more easily extended to flight conditions outside the range of test data, often each element of the scheme does not have the same range of validity as other elements. Examples of component build-up codes include; McCoy's combination of Van Dyke hybrid theory with Van Driest boundary-layer theory,¹⁸ the USAF Missile DATCOM code,¹⁹ and the Naval Surface Warfare Center Aerodynamics Prediction (NSWC-AP) code.²⁰ Application of the DATCOM and NSWC-AP codes to both spin-stabilized and fin-stabilized projectiles has been evaluated by Vukelich and Jenkins,²¹ Sun and Cummings,²² and Mikhail.²³

Viscous-inviscid interaction theory is essentially an extension of the Euler/boundary-layer theories. Euler/boundary-layer theory uses a solution procedure for the inviscid (Euler) flow equations to determine the edge velocity boundary condition for the boundary-layer solution. Once the boundary layer has been computed, the inviscid procedure is used

⁸ McCoy, R.L., "McDAG - A Computer Program for Estimating the Drag Coefficients of Projectiles," BRL-TR-2293, U.S. Army Ballistic Research Laboratory, Aberdeen Proving Ground, MD, Feb. 1981.

⁹ Donovan, W.F., and Wood, S.A., "Automatic Plotting Routines for Estimating Aerodynamic Properties of Spin Stabilized Projectiles in Flat Fire Trajectories at $2 < M < 5$," BRL-MR-3204, U.S. Army Ballistic Research Laboratory, Aberdeen Proving Ground, MD, Oct. 1982.

¹⁰ Donovan, W.F., "Hypothetical Zero Yaw Drag Trajectory of Spinning Projectiles Between $M=5$ and $M=10$," BRL-MR-3404, U.S. Army Ballistic Research Laboratory, Aberdeen Proving Ground, MD, Nov. 1984.

¹¹ Morris, M.A., "A Computer Program to Predict the Major Aerodynamic Coefficients of Conventional Shell and Bullet Body Shapes," RARDE Memorandum Report 9/81, June 1981.

¹² Donovan, W.F., Nusca, M.J., and Wood, S.A., "Automatic Plotting Routines for Estimating Static Aerodynamic Properties of Long Rod Finned Projectiles for $2 \leq M \leq 5$," BRL-MR-3123, U.S. Army Ballistic Research Laboratory, Aberdeen Proving Ground, MD, Aug. 1981.

¹³ Donovan, W.F., and Grollman, B.B., "Procedure for Estimating Zero Yaw Drag Coefficient for Long Rod Projectiles at Mach Numbers from 2 to 5," BRL-MR-2819, U.S. Army Ballistic Research Laboratory, Aberdeen Proving Ground, MD, Mar. 1978.

¹⁴ Donovan, W.F., "Automatic Plotting Routines for Estimating Static Aerodynamic Properties of Flared Projectiles for $2 < M < 5$," BRL-MR-3579, U.S. Army Ballistic Research Laboratory, Aberdeen Proving Ground, MD, Mar. 1987.

¹⁵ Whyte, R.H., "SPIN-73, An Updated Version of the SPINNER Computer Program," U.S. Army Picatinny Arsenal Technical Report TR-4588, November 1973.

¹⁶ Whyte, R.H., Burnett, J.R., and Hathaway, W.H., "FIN-81 A Computer Program to Predict Fin Stabilized Projectile Aerodynamic Coefficients and Stability Parameters," General Electric Armament Systems Dept., April 1981.

¹⁷ Fischer, M.A., "PRODAS User Manual - Version 3.1," General Electric Armament Systems Dept., February 1989.

¹⁸ McCoy, R.L., "Estimation of the Static Aerodynamic Characteristics of Ordnance Projectiles at Supersonic Speeds," BRL Report No. 1682, U.S. Army Ballistic Research Laboratory, Aberdeen Proving Ground, MD, Nov. 1979.

¹⁹ Vukelich, S.R., and Jenkins, J.E., "Missile Datcom: Aerodynamic Prediction of Conventional Missiles Using Component Build-Up Techniques," AIAA-84-0988, 1984.

²⁰ Devan, L., and Mason, L.A., "Aerodynamics of Tactical Weapons to Mach Number 8 and Angle of Attack 180°: Part II, Computer Program and Users Guide," NSWC TR 81-358, Naval Surface Warfare Center, Sept. 1981.

²¹ Vukelich, S.R., and Jenkins, J.E., "Evaluation of Component Buildup Methods for Missile Aerodynamic Prediction," AIAA Journal of Spacecraft and Rockets, Vol. 19, No. 6, Nov/Dec 1982, pp. 481-488.

²² Sun, J., and Cummings, R.M., "Evaluation of Missile Aerodynamic Characteristics Using Rapid Prediction Techniques," AIAA Journal of Spacecraft and Rockets, Vol. 21, No. 6, Nov/Dec 1984, pp. 513-520.

²³ Mikhail, A.G., "Interactive Input for Projectile Fast Design Codes Package," BRL-MR-3631, U.S. Army Ballistic Research Laboratory, Aberdeen Proving Ground, MD, October 1987.

to recompute the flow over the original body combined with the boundary layer displacement thickness. The procedure is uncoupled and does not recompute the boundary layer. A version of Euler/boundary-layer theory has been applied to spin-stabilized projectiles in transonic and supersonic flight by Sturek, Nietubicz, and others.²⁴⁻²⁶ The code by Sturek et.al.²⁴ computes the inviscid (Euler) flow over a projectile using a finite-difference MacCormack technique. The effect of the boundary layer on the flowfield adjacent to the surface of the body is accounted for by adding the local displacement thickness to the local body radius and solving the inviscid flowfield with an adjusted boundary condition. The present code, INTERACT, includes an interaction model for the viscous and inviscid theories allowing the independent solutions to be coupled. Thus, the resulting flowfield represents a solution to the boundary-layer equations and the Euler equations simultaneously. The use of an inverse solution to the boundary-layer equations (i.e. specified boundary layer displacement thickness and computed edge velocity) is a necessary element of the procedure. Similar techniques have been successfully used for airfoils in low speed flow.²⁷⁻³⁰ The application of this method to supersonic flow is outlined by Nusca⁷ and described in Section III.3 of this report.

Aerodynamic heating analysis for projectiles flying at Mach number 5 was examined by Sedney³¹ in 1958. This analysis assumed that the projectile geometry can be represented by two-dimensional components for which approximate values of the heat transfer coefficient have been documented by Van Driest.³² This analysis yielded the surface temperature versus time of flight (or range) for small L/D, spin-stabilized projectiles. Since then multi-dimensional analyses and rigorous experimental tests have yielded closed form formulae for the calculation of heat transfer coefficients on general axisymmetric geometries. These formulae relate surface heat transfer to computed (or measured) boundary layer profiles and boundary layer edge flow properties (i.e. velocity, pressure, entropy). Some examples of this work include Rubesin and Johnson,³³ Young and Janssen,³⁴ Eckert,³⁵ Fay and Kemp,³⁶ Crabtree et.al.,³⁷ Fancett,³⁸ DeJarnette et.al.,³⁹ and recently Hoffmann et.al.⁴⁰ In particular, Fancett³⁸ and Hoffmann⁴⁰ have assembled engineering heat transfer formulae and applied these methods to axisymmetric projectile configurations. The work of Fancett³⁸ is used here (Section IV) to compute surface heat transfer coefficients from

²⁴ Sturek, W.B., Dwyer, H.A., Kayser, L.D., Nietubicz, C.J., Reklis, R.P., and Opalka, K.O., "Computations of Magnus Effects for a Yawed, Spinning Body of Revolution," *AIAA Journal*, Vol. 16, No. 7, July 1978, pp. 687-692.

²⁵ Sturek, W.B., Mylin, D.C., and Bush, C.C., "Computational Parametric Study of the Aerodynamics of Spinning Slender Bodies at Supersonic Speeds," *AIAA-80-1585, Proceedings of the 7th AIAA Atmospheric Flight Mechanics Conference*, August 11-13, 1980.

²⁶ Nietubicz, C.J., Danberg, J.E., and Inger, G.R., "A Theoretical and Experimental Investigation of a Transonic Projectile Flow Field," *BRL-MR-3291, U.S. Army Ballistic Research Laboratory, Aberdeen Proving Ground, MD.*, July 1983.

²⁷ Pletcher, R.H., "Prediction of Incompressible Turbulent Separating Flow," *Journal of Fluids Engineering*, Vol. 100, Dec. 1978, pp. 427-433.

²⁸ Kwon, O., and Pletcher, R.H., "Prediction of Incompressible Separated Boundary Layers Including Viscous-Inviscid Interaction," *Transactions of the ASME*, Vol. 101, Dec. 1979, pp. 466-472.

²⁹ Williams, B.R., "The Prediction of Separated Flow Using A Viscous-Inviscid Interaction Method," *Aeronautical Journal*, May 1985, pp. 185-197.

³⁰ Im, B.J., "A Coupled Viscid-Inviscid Calculation Method for the Prediction of Unsteady Separated Flows Over An Airfoil," *AIAA-88-0566, Proceedings of the 26th AIAA Aerospace Sciences Meeting, Reno NV*, Jan. 11-14, 1988.

³¹ Sedney, R., "Aerodynamic Heating Problems In Shell Design," *BRL Report No. 1049, U.S. Army Ballistic Research Laboratory, Aberdeen Proving Ground, MD*, March 1958.

³² Van Driest, E.R., "The Problem of Aerodynamic Heating," *Aeronautical Engineering Review*, Vol. 15, No. 10, October 1956, pp. 26-41.

laminar and turbulent flow profiles as determined by the INTERACT code.

Table 1. AERODYNAMIC DESIGN CODES FOR AXISYMMETRIC BODIES

Code	Inviscid Methods	Boundary Layer Methods	Inviscid/BL Interaction	Heat Transfer
MCDRAG ⁸	Similarity rules	Flat plate empirical	None	None
Donovan, Wood ⁹	Empirical data curve fits	Flat plate empirical	None	None
Donovan (flare) ¹⁴	Empirical data curve fits	Flat plate empirical	None	None
McCoy ¹⁸	Van Dyke hybrid, Linear potential	Van Driest flat plate theory	Single iteration	None
DATCOM ¹⁹	Component build-up Slender body theory	Flat plate empirical	None	None
NSWC-AP ²⁰	Van Dyke hybrid, 2nd-order Shock/Exp, Newtonian theory	Van Driest flat plate theory	None	None
INTERACT	Linearized perturbation, 2nd-order Shock/Exp with flare corrections, Newtonian theory	2D/Axisymmetric 2nd-order finite difference solution	Multiple iteration w/convergence criteria	Algebraic, assumes chemical equilibrium
(No attempt made to include all available codes)				

³³ Rubesin, M.W., and Johnson, H.A., "A Critical Review of Skin-Friction and Heat-Transfer Solutions of the Laminar Boundary Layer of a Flat Plate," Transactions of the ASME, Vol. 71, No. 4, May 1949, pp. 358-388.

³⁴ Young, G.B., and Janssen, E., "The Compressible Boundary Layer," Journal of Aeronautical Sciences, Vol. 19, April 1952, pp. 229-236.

³⁵ Eckert, E.R., "Engineering Relations for Friction and Heat Transfer to Surfaces in High Velocity Flow," Journal of Aeronautical Sciences, Vol. 22, No. 8, August 1955, pp. 585-587.

³⁶ Fay, J.A., and Kemp, N.H., "Theory of Stagnation-Point Heat Transfer in a Partially Ionized Diatomic Gas," AIAA Journal, Vol. 1, No. 12, Dec. 1963, pp. 2741-2751.

³⁷ Crabtree, L.F., Dommett, R.L., and Woodley, J.G., "Estimation of Heat Transfer to Flat Plates, Cones and Blunt Bodies," RAE TR No. 3637, July 1965.

³⁸ Fancett, R.K., "Heat Transfer to Slender Projectiles at Mach Numbers Between 5 and 10," RARDE Memorandum Report 2/70, 1970.

³⁹ DeJarnette, F.R., Hamilton, H.H., Weilmuenster, K.J., and Cheatwood, F.M., "A Review of Some Approximate Methods Used in Aerodynamic Heating Analyses," AIAA Journal of Thermophysics, Vol. 1, No. 1, Jan. 1987, pp. 5-12.

⁴⁰ Hoffman, K.A., Wilson, D.E., and Hamburger, C., "Aerothermodynamic Analyses of Projectiles at Hypersonic Speeds," AIAA-2185, Proceedings of the 7th AIAA Applied Aerodynamics Conference, Seattle WA, July 31 to August 2, 1989.

III. INTERACTION MODEL

1. Inviscid Methods

The inviscid flowfield is governed by the Euler equations (i.e. Navier-Stokes equations with zero kinematic viscosity or infinite Reynolds number) which describe the conservation of mass, momentum and energy for a compressible flow.

$$\frac{\partial \rho}{\partial t} + \nabla \cdot (\rho \vec{V}) = 0 \quad (1)$$

$$\rho \frac{D \vec{V}}{Dt} = -\nabla p \quad (2)$$

$$\rho \frac{D}{Dt} \left(e + \frac{V^2}{2} \right) = -\nabla \cdot (p \vec{V}) \quad (3)$$

These equations can be solved by finite-difference techniques requiring extensive computational resources. However, finite-difference methods are not the preferred choice for aerodynamic design codes since, for general geometries, grid generation requires skilled interaction between the code and operator. Previous aerodynamic design codes have utilized linearized perturbation, shock-expansion, and modified-Newtonian theories to solve the inviscid flowfield (see Table 1). These methods are suitable choices for the present code, since they yield accurate solutions when applied within the limits of each theory, do not require grid generation, and run for less than one minute CPU time on minicomputers. Linearized perturbation and shock-expansion theories are limited to pointed slender bodies, while the limits on freestream Mach number and flow deflection angle for each theory are quite different. Linearized perturbation methods are based on linearized solutions of Equations 1-3 written in velocity potential form. Shock-expansion theory is based on an assumption of locally two-dimensional flow with a correction for axisymmetric effects. For a flared afterbody, a special correction is required. Linearized perturbation theory is more generally applicable to irregular body shapes, but imposes greater restrictions on the body fineness ratio and freestream Mach number than does shock-expansion theory. Modified-Newtonian theory can be applied on the forebody section of projectiles with blunt cone or blunt ogive geometries.

Based on the freestream Mach number, the INTERACT code employs the most suitable method or combination of methods for a given projectile geometry, thus accounting for most cases of interest to the projectile designer. These methods are reviewed in the following subsections.

a. Linearized Perturbation Theory

Assuming that the flowfield over the body is steady and irrotational, then $\frac{\partial}{\partial t} = 0$ and $\nabla \times \vec{V} = 0$. It can be shown,⁴¹ that Equation 2 reduces to

$$dp = -\rho V dV \quad (4)$$

The irrotational flow assumption is exactly true for the flow behind an attached oblique shock wave on a wedge, and approximately true for a sharp-nose slender body in supersonic flow. If the slender body is moving supersonically, the attendant shock wave will be slightly curved, and hence, strictly speaking, the flowfield will be slightly rotational. However, it is usually practical to assume $\nabla \times \vec{V} \approx 0$ for such cases. It is then convenient to define a velocity potential, Φ , such that $\vec{V} \equiv \nabla \Phi$ where $\nabla \times \vec{V} = \nabla \times \nabla \Phi = 0$, with Φ a scalar. Application to the continuity equation (Equation 1) and to Euler's equation (Equation 4) for isentropic flow (i.e. $dp/d\rho = a^2$), yields the Velocity Potential Equation:

$$(1 - \frac{\Phi_x^2}{a^2})\Phi_{xx} + (1 - \frac{\Phi_y^2}{a^2})\Phi_{yy} + (1 - \frac{\Phi_z^2}{a^2})\Phi_{zz} - 2\frac{\Phi_x\Phi_y}{a^2}\Phi_{xy} - 2\frac{\Phi_x\Phi_z}{a^2}\Phi_{xz} - 2\frac{\Phi_y\Phi_z}{a^2}\Phi_{yz} = 0 \quad (5)$$

where

$$\begin{aligned} a^2 &= a_t^2 - \frac{\gamma-1}{2}(\Phi_x^2 + \Phi_y^2 + \Phi_z^2), \text{ the local speed of sound} \\ a &= \text{the total speed of sound, constant for a calorically perfect gas} \end{aligned}$$

The Velocity Potential Equation (Equation 5) is a non-linear partial differential equation that is exact within the framework of irrotational, isentropic flow. It applies to all values of the Mach number. Equation 5 can be applied to a slender body in uniform flow where the freestream velocity (V_∞) is only slightly disturbed (perturbed). The analysis of this type of flowfield is referred to as small-perturbation theory. The body causes a disturbance of the uniform flow and the velocity is written in terms of the perturbed velocity components, $\tilde{u}, \tilde{v}, \tilde{w}$, in the x, y, z directions where $\nabla \Phi = \vec{V} = (V_\infty + \tilde{u})\hat{i} + (\tilde{v})\hat{j} + (\tilde{w})\hat{k}$. The perturbed velocity potential, $\tilde{\Phi}$, is defined using:

$$\Phi(x, y, z) = V_\infty x + \tilde{\Phi}(x, y, z)$$

Substituting this expression into Equation 5, we obtain the velocity potential equation for the perturbed flow:

$$\begin{aligned} (1 - M_\infty^2) \frac{\partial \tilde{u}}{\partial x} + \frac{\partial \tilde{v}}{\partial y} + \frac{\partial \tilde{w}}{\partial z} &= M_\infty^2 \left((\gamma + 1) \frac{\tilde{u}}{V_\infty} + \frac{(\gamma + 1)}{2} \frac{\tilde{u}^2}{V_\infty^2} + \frac{(\gamma - 1)}{2} \left(\frac{\tilde{v}^2 + \tilde{w}^2}{V_\infty^2} \right) \right) \frac{\partial \tilde{u}}{\partial x} \\ &+ M_\infty^2 \left((\gamma - 1) \frac{\tilde{u}}{V_\infty} + \frac{(\gamma + 1)}{2} \frac{\tilde{v}^2}{V_\infty^2} + \frac{(\gamma - 1)}{2} \left(\frac{\tilde{w}^2 + \tilde{u}^2}{V_\infty^2} \right) \right) \frac{\partial \tilde{v}}{\partial y} \\ &+ M_\infty^2 \left((\gamma - 1) \frac{\tilde{u}}{V_\infty} + \frac{(\gamma + 1)}{2} \frac{\tilde{w}^2}{V_\infty^2} + \frac{(\gamma - 1)}{2} \left(\frac{\tilde{u}^2 + \tilde{v}^2}{V_\infty^2} \right) \right) \frac{\partial \tilde{w}}{\partial z} \\ &+ M_\infty^2 \left(\frac{\tilde{v}}{V_\infty} \left(1 + \frac{\tilde{u}}{V_\infty} \right) \left(\frac{\partial \tilde{u}}{\partial y} + \frac{\partial \tilde{v}}{\partial x} \right) + \frac{\tilde{w}}{V_\infty} \left(1 + \frac{\tilde{u}}{V_\infty} \right) \left(\frac{\partial \tilde{u}}{\partial z} + \frac{\partial \tilde{w}}{\partial x} \right) \right) \\ &+ M_\infty^2 \left(\frac{\tilde{v}\tilde{w}}{V_\infty^2} \left(\frac{\partial \tilde{w}}{\partial y} + \frac{\partial \tilde{v}}{\partial z} \right) \right) \end{aligned} \quad (6)$$

where

⁴¹ Anderson, J.D., Modern Compressible Flow with Historical Perspective, McGraw-Hill, 1982.

$$\begin{aligned} a^2 &= a_\infty^2 - \frac{\gamma-1}{2}(2\tilde{u}V_\infty + \tilde{u}^2 + \tilde{v}^2 + \tilde{w}^2) \\ M_\infty &= V_\infty/a_\infty \end{aligned}$$

Assuming that \tilde{u} , \tilde{v} , and \tilde{w} are small compared to V_∞ , then $\tilde{u}/V_\infty, \tilde{v}/V_\infty, \tilde{w}/V_\infty \ll 1$ and $(\tilde{u}/V_\infty)^2, (\tilde{v}/V_\infty)^2, (\tilde{w}/V_\infty)^2 \ll 1$. We can therefore exclude from Equation 6 the term $M_\infty^2(\gamma+1)(\tilde{u}/V_\infty)\partial\tilde{u}/\partial x$ in favor of $(1-M_\infty^2)\partial\tilde{u}/\partial x$ except when $M_\infty \simeq 1$ and the terms $M_\infty^2(\gamma-1)(\tilde{u}/V_\infty)\partial\tilde{v}/\partial y$ and $M_\infty^2(\gamma-1)(\tilde{u}/V_\infty)\partial\tilde{w}/\partial z$ in favor of $\partial\tilde{v}/\partial y$ and $\partial\tilde{w}/\partial z$, respectively, for $M_\infty \leq 5$ (approximately). We then obtain the Prandtl-Glauert equation:

$$(1 - M_\infty^2) \frac{\partial^2 \tilde{\Phi}}{\partial x^2} + \frac{\partial^2 \tilde{\Phi}}{\partial y^2} + \frac{\partial^2 \tilde{\Phi}}{\partial z^2} = 0 \quad (7)$$

or in axisymmetric form ($\tilde{w} = 0$),

$$\beta^2 \frac{\partial^2 \tilde{\Phi}}{\partial x^2} - \frac{\partial^2 \tilde{\Phi}}{\partial r^2} - \frac{1}{r} \frac{\partial^2 \tilde{\Phi}}{\partial r^2} = 0 \quad (8)$$

where, $\beta = \sqrt{M_\infty^2 - 1}$

Equation 8 is a linear equation that is valid for inviscid, irrotational, isentropic flow with small perturbations to the freestream flowfield. In addition, flows for which $.8 \leq M_\infty \leq 1.2$ and $M_\infty \geq 5$ (approximately) have been excluded. Von Karman and Moore⁴² showed that Equation 8 can be solved by placing a source distribution along the axis of the body and using the method of superposition of elementary solutions. This method is restricted to axisymmetric flow (i.e. the body is at zero incidence and $\tilde{w} = 0$). The source strength of each element is $f(\xi)d\xi$, located at $x = \xi + \beta r$. Integration over all sources for the entire length of the body ($x = 0$ to L) yields the following relation for the perturbed velocity potential:

$$\tilde{\Phi}(x, r) = \int_{-\infty}^{\xi} \frac{f(\xi)d\xi}{\sqrt{(x - \xi)^2 - \beta^2 r^2}} = \int_0^{x - \beta r} \frac{f(\xi)d\xi}{\sqrt{(x - \xi)^2 - \beta^2 r^2}} \quad (9)$$

where, $r = \sqrt{y^2 + z^2}$; the radial distance from the axis of the body.

Equation 9 applies to a pointed body where $f(\xi) = 0$ for $\xi \leq 0$ ($x \leq 0$). The change in the limits of integration is a consequence of the imaginary contribution to $\tilde{\Phi}$ if $\xi > x - \beta r$ (i.e. the influence of sources downstream of x is not considered for purely supersonic flow). Using the transformation $\xi = x - \beta r \cosh \sigma$, $d\xi = \sqrt{(x - \xi)^2 - \beta^2 r^2} d\sigma$ and applying the method of superposition of elementary solutions (i.e. $f'(\xi) = A_i = \text{constant}$ for $\xi_{i-1} < \xi < \xi_i$, dividing the body axis into n simple parts ($i = 1, \dots, n$) and imposing separate sources in these parts), the velocity components, \tilde{u}, \tilde{v} , are then expressed as⁴²

$$\tilde{u}(x_i, r_i) = \sum_{j=1}^i A_j \left(\cosh^{-1} \frac{x_i - \xi_j}{\beta r_i} - \cosh^{-1} \frac{x_i - \xi_{j-1}}{\beta r_i} \right) \quad (10)$$

⁴² Liepmann, H.W., and Rosko, R.A., Elements of Gasdynamics, Wiley, NY, 1957 (pp. 227-230).

$$\tilde{v}(x_i, r_i) = - \sum_{j=1}^i \frac{A_j}{r_i} \left(\sqrt{(x_i - \xi_j)^2 - \beta^2 r_i^2} - \sqrt{(x_i - \xi_{j-1})^2 - \beta^2 r_i^2} \right) \quad (11)$$

where, $\xi_j = x_j - \beta r_j$ and $A_j = f'(\xi_j) = \text{constant}$.

Combining Equations 10 and 11 with a tangent flow boundary condition on the body surface, $dr_i/dx_i = \tilde{v}_i/(V_\infty + \tilde{u}_i)$ yields a system of three linear equations for the unknowns $\tilde{u}(x_i, r_i)$, $\tilde{v}(x_i, r_i)$, and A_i . Since A_i is a function of A_j for $j = 1, \dots, i-1$, the solution is marched from $A_1 = 0$ at $x = 0$ to $x = x_i$. The solution must be started from the nose of the body. Application of Equations 10 and 11 for the solution of the inviscid flow over a slender body has been termed linearized perturbation theory. The mathematics of Equations 10 and 11 dictate the following condition for the flow deflection caused by the body nose angle (δ_n). For $i = 2$:

$$\begin{aligned} \tilde{u}_2 &= A_2(-\cosh^{-1}[(x_2 - \xi_1)/(\beta r_2)]) \\ \tilde{v}_2 &= -A_2 \left(-\sqrt{(x_2 - \xi_1)^2 - \beta^2 r_2^2} \right) \end{aligned}$$

Therefore, $(x_2 - \xi_1)/(\beta r_2) \geq 1$ and $(x_2 - \xi_1)^2 - \beta^2 r_2^2 \geq 0$ and thus

$$\frac{1}{\beta \tan \delta_n} \geq 1 \quad (12)$$

Since the solution must be started from the nose of the body, Equation 12 determines the range of applicability of the theory, assuming that the flow remains attached to the body. Equation 12 is equivalent to the limit $\delta_n \leq \tilde{\mu} = \arcsin(1/M_\infty)$ (i.e. that the freestream Mach number lines reside outside the body surface). Figure 1 displays this limit for $1 \leq M_\infty \leq 10$.

Other body surface flow properties, C_{p_i} (local pressure coefficient), V_i/V_∞ (local tangential velocity), and ρ_i/ρ_∞ (local flow density) can be obtained from

$$C_{p_i} = \frac{2}{\gamma M_\infty^2} \left(\frac{p_i}{p_n} \frac{p_n}{p_\infty} - 1 \right) \quad , \quad \frac{p_i}{p_n} = \left(\frac{1 + \frac{\gamma-1}{2} M_n^2}{1 + \frac{\gamma-1}{2} M_i^2} \right)^{\frac{1}{\gamma-1}} \quad (13)$$

$$V_i = \sqrt{u_i^2 + v_i^2} = M_i a_i = M_i a_\infty \sqrt{\frac{1 + \frac{\gamma-1}{2} M_\infty^2}{1 + \frac{\gamma-1}{2} M_i^2}} \quad , \quad \frac{V_i}{V_\infty} = \frac{M_i}{M_\infty} \sqrt{\frac{1 + \frac{\gamma-1}{2} M_\infty^2}{1 + \frac{\gamma-1}{2} M_i^2}} \quad (14)$$

$$\frac{\rho_i}{\rho_\infty} = \frac{(p_i/p_\infty) p_\infty \gamma}{\rho_\infty M_i^2 V_i^2} \quad (15)$$

where, M_n and p_n are the Mach number and pressure behind the nose shock (see Equ 18 and 19).

b. Second-Order Shock-Expansion Theory

Solutions of the inviscid flow about simple geometries can be obtained easily if the flowfield consists entirely of shock waves and/or expansion waves. For generalized (i.e.

first-order) shock-expansion theory, the flow over an axisymmetric body at zero incidence to the freestream is assumed to be locally two dimensional. Therefore, the continuity equation (Equation 1) is only approximately satisfied. Shock waves are assumed to be oblique, straight, and attached to the body. Body surface properties of the flow (pressure, Mach number, and density) can be obtained by application of the oblique shock relations for the flow behind a shock wave attached to the nose of the body, and the Prandtl-Meyer function for compressions and expansions caused by changes in body slope downstream of the nose. Eggers et.al.⁴³ documented the generalized shock-expansion theory for supersonic flow. Second-order shock-expansion theory was proposed by Syvertson and Dennis⁴⁴ to correct the first-order results for non-isentropic and axisymmetry effects.

In general, an oblique shock wave is three-dimensional and curved. However, it is usually sufficient to consider the flow at an arbitrary point to be locally two-dimensional and the shock to be straight. It is then possible to derive the oblique shock relations from Equations 1-3 together with the requirement that the entropy (s) does not decrease. The gas is assumed to be adiabatic and perfect. The total enthalpy (h_t), total temperature (T_t), total pressure (p_t), and total speed of sound (a_t) are constant across the shock. All oblique shock relations used in this section are derived in Reference 45.

The Prandtl-Meyer function for an isentropic flow expansion is used to determine the flowfield properties downstream of a curved surface (convex or concave) where shocks are not involved. Locally two-dimensional flow is assumed. This function can be used over a sharp concave corner (e.g. cylinder-flare junction), although it is not formally valid since the flow is not isentropic. As a result, a second-order correction is required and will be discussed latter in this section. For a perfect gas, the Prandtl-Meyer angle, ν , through which the stream turns in expanding from $M = 1$ to a supersonic Mach number, M , is given in Reference 45 as

$$\nu = \sqrt{\frac{\gamma + 1}{\gamma - 1}} \arctan \sqrt{\frac{\gamma - 1}{\gamma + 1} (M^2 - 1)} - \arctan \sqrt{M^2 - 1} \quad (16)$$

For first-order shock-expansion theory, we begin the inviscid flowfield solution at the nose of the body. For a nose half-angle, δ_n , and freestream Mach number, M_∞ , the shock wave half-angle, θ_n , the Mach number behind the shock, M_n , and the static pressure jump across the shock, p_n/p_∞ , can be determined from the oblique shock relations:⁴⁵

$$\cot \delta_n = \tan \theta_n \left(\frac{(\gamma + 1)M_\infty^2}{2(M_\infty^2 \sin^2 \theta_n - 1)} - 1 \right) \quad (17)$$

$$M_n^2 = \frac{(\gamma + 1)^2 M_\infty^4 \sin^2 \theta_n - 4(M_\infty^2 \sin^2 \theta_n - 1)(\gamma M_\infty^2 \sin^2 \theta_n + 1)}{[2\gamma M_\infty^2 \sin^2 \theta_n - (\gamma - 1)][(\gamma - 1)M_\infty^2 \sin^2 \theta_n + 2]} \quad (18)$$

$$\frac{p_n}{p_\infty} = \frac{2\gamma M_\infty^2 \sin^2 \theta_n - (\gamma - 1)}{\gamma + 1} \quad (19)$$

⁴³ Eggers, A.J., Savin, R.C., and Syvertson, C.A., "The Generalized Shock-Expansion Method and Its Application to Bodies Traveling at High Supersonic Airspeeds," *Journal of Aeronautical Sciences*, Vol. 22, No. 4, April 1955, pp. 231-238.

⁴⁴ Syvertson, C.A., and Dennis, D.H., "A Second-Order Shock-Expansion Method Applicable to Bodies of Revolution Near Zero Lift," *NACA TN-3527*, Jan. 1956.

⁴⁵ Ames Research Staff, "Equations, Tables, and Charts for Compressible Flow," *NACA Report-1135*, NASA Ames Aeronautical Laboratory, Moffet Field CA, 1958.

Equation 17 is solved iteratively. The shock wave must be attached to the nose of the body so that $0 \leq \delta_n \leq \delta_{\max}$, where δ_{\max} is determined iteratively from the following equations:⁴⁵

$$\sin^2 \theta_{\max} = \frac{(\gamma + 1)M_{\infty}^2 - 4 + \sqrt{(\gamma + 1)[(\gamma + 1)M_{\infty}^4 + 8(\gamma - 1)M_{\infty}^2 + 16]}}{4\gamma M_{\infty}^2} \quad (20)$$

$$\cot \delta_{\max} = \tan \theta_{\max} \left(\frac{(\gamma + 1)M_{\infty}^2}{2(M_{\infty}^2 \sin^2 \theta_{\max} - 1)} - 1 \right) \quad (21)$$

Figure 2 shows the nose half-angle limit, δ_{\max} , for $1 \leq M_{\infty} \leq 10$.

A value for ν_n is obtained using Equation 16 and M_n . For all body points, i , downstream of the nose, $\nu_i = \delta_n - \delta_i + \nu_n$, where δ_i is the local body slope. Since, $\nu_i = f(M_i)$, Equation 16 can be used iteratively to obtain the value of M_i , the local Mach number. Other body surface flow properties, C_{p_i} (local pressure coefficient), V_i/V_{∞} (local tangential velocity), and ρ_i/ρ_{∞} (local flow density) can be obtained from Equations 13-15.

The second-order theory⁴⁴ accounts for non-isentropic and axisymmetric effects using the first-order results, denoted with the subscript s (e.g. p_s and M_s).

$$p_i = p_{\text{cone}_i} - (p_{\text{cone}_i} - p_{s_i}) \exp(-\zeta \psi) \quad (22)$$

$$\zeta = (x_i \sin \delta_n - r_i \cos \delta_n) / (r_i \cos \delta_i - x_i \sin \delta_i) \quad (23)$$

$$\psi = \frac{\gamma p_{s_i} M_{s_i}^2}{2(M_{s_i}^2 - 1)(p_{\text{cone}_i} - p_{s_i})} \left(\frac{\Omega_n}{\Omega_{s_i}} - \frac{\sin \delta_i}{\sin \delta_n} \right) \quad (24)$$

$$\Omega = \frac{1}{M} \left(\frac{1 + \left(\frac{\gamma-1}{2} \right) M^2}{(\gamma + 1)/2} \right)^{\frac{\gamma+1}{2(\gamma-1)}} \quad (25)$$

where p_{cone_i} is the pressure on a cone of half-angle δ_i for M_{∞} (see III.1.c).

For flare afterbodies, allowance must be made for the non-isentropic nature of the flow thru the shock wave. Robinson⁴⁶ derived a second-order correction for flares with the assumption that $\partial p / \partial x = 0$ at the cylinder-flare junction, thus restricting these results to bodies with long cylinder sections.

The effect of axisymmetric flow on flare pressure values, p_i , is computed using an exponential curve fitted to the pressure gradient downstream of the cylinder-flare junction, $(\partial p / \partial x)_F$.

$$p_i = p_{\text{cone}_F} - (p_{\text{cone}_F} - p_{s_F}) \exp(-\eta) \quad (26)$$

$$\eta = \left(\frac{\partial p}{\partial x} \right)_F \left(\frac{x - x_F}{(p_{\text{cone}_F} - p_{s_F}) \cos \delta_F} \right) \quad (27)$$

$$\left(\frac{\partial p}{\partial x} \right)_F = - \left(\frac{1}{3 - \tan \tilde{\mu}_F / \tan(\theta_F - \delta_F)} \right) \frac{2B_F}{r} \sin \delta_F \quad (28)$$

⁴⁶ Robinson, M.L., "Boundary Layer Effects in Supersonic Flow Over Cylinder-Flare Bodies," WRE-Report-1238, Australian Defense Scientific Service, Weapons Research Establishment, July 1974.

where

x_F = the location of the cylinder-flare junction from the nose of the body
 p_{s_F} = pressure downstream of the flare shock (two-dimensional calculation)
 M_{s_F} = Mach number downstream of the flare shock (two-dimensional calculation)
 p_{cone_F} = cone pressure using flare angle δ_F
 $\tilde{\mu}_F$ = $\arcsin(1/M_{s_F})$
 B_F = $\gamma p_{s_F} M_{s_F}^2 / [2(M_{s_F}^2 - 1)]$
 θ_F = shock wave half-angle on a wedge of half-angle δ_F and for M_∞

c. Cone Surface Pressure

Both linearized perturbation and second-order shock-expansion theories require an accurate calculation procedure for the cone surface pressure at the nose of the body. Second-order shock-expansion theory requires cone pressure calculations for additional body angles. Due to the frequency at which cone pressures must be evaluated for a given body, fast but accurate calculation methods must replace advanced cone flow theories, such as that of Taylor and MacColl.⁴⁷

First-order slender-body theory is accurate for cone half-angles, $\delta \leq 5^\circ$ in supersonic flow ($M_\infty \leq 4$) and prescribes the cone surface pressure coefficient as

$$C_p = 2\delta^2 \left(\log \frac{2}{\beta\delta} - \frac{1}{2} \right) \quad (29)$$

Second-order slender-body theory is accurate for $\delta \leq 10^\circ$ in supersonic flow ($M_\infty \leq 4$) and imposes a mathematical limit on δ and M_∞ (Note: $\cot \delta / \beta \geq 1$ and $\cot^2 \delta - \beta^2 \geq 0$) similar to linearized perturbation theory (see Equation 12). The cone surface pressure is prescribed as

$$C_p = -\frac{2u}{V_\infty} - \left(\frac{v}{V_\infty} \right)^2 \quad (30)$$

where

$u = -a \cosh^{-1} \left(\frac{\cot \delta}{\beta} \right)$
 $v = a \sqrt{\cot^2 \delta - \beta^2}$
 $a = V_\infty \tan \delta / [\sqrt{\cot^2 \delta - \beta^2} + \tan \delta \cosh^{-1}(\cot \delta / \beta)]$

Linearized perturbation theory could also be used. However, slender-body theory (Equ. 29-30) as well as linearized perturbation theory have limitations in flow deflection angle and Mach number that are unacceptable for a general projectile design code. Two-dimensional shock theory for surface pressure on a wedge is more general (see Figure 2), but does not include the necessary axisymmetric effects that are present in cone flow. A method that corrects the wedge theory for a cone would be the best choice. Using Equations 17 thru 19 for the wedge theory and Reference 47 for the cone theory, Figure

⁴⁷ Taylor, G.I., and MacColl, J.W., "The Air Pressure on a Cone Moving at High Speed," Proc. Royal Soc. (London), Ser. A, Vol. 179, pp. 278-311.

3 shows $C_{p_{cone}}/C_{p_{wedge}}$ vs. $\log_{10}(M_\infty \delta)$ for $5^\circ \leq \delta \leq 30^\circ$ and $2 \leq M_\infty \leq 10$. The data can be fitted by a fifth-order polynomial using a least-squares technique. Thus $C_{p_{cone}}$ can be determined from $C_{p_{wedge}}(C_{p_{cone}}/C_{p_{wedge}})$.

d. Modified-Newtonian Theory

The local pressure coefficient at a point i on the body can be estimated from the freestream Mach number, M_∞ , ratio of specific heats, γ , and the local body surface inclination, δ_i , using⁴⁸

$$C_{p_i} = (C_p)_{\max} \sin^2 \delta_i \quad (31)$$

$$(C_p)_{\max} = \frac{2}{\gamma M_\infty^2} \left[\left(\frac{(\gamma + 1)^2 M_\infty^2}{4\gamma M_\infty^2 - 2(\gamma - 1)} \right)^{\gamma/(\gamma-1)} \left(\frac{1 - \gamma + 2\gamma M_\infty^2}{\gamma + 1} \right) - 1 \right] \quad (32)$$

The body surface inclination angle is given by $\sin \delta_i = (\vec{V}_\infty / |V_\infty|) \cdot \hat{n}$. Other body surface flow properties at point i on the body are obtained from C_{p_i} , p_n , and M_n where subscript n denotes static flow properties behind the projectile nose shock.

$$\frac{\rho_i}{\rho_\infty} = \frac{C_{p_i}(\rho_\infty V_\infty^2/2) + p_\infty}{p_\infty \left(\frac{1 + ((\gamma - 1)/2)M_n^2}{1 + ((\gamma - 1)/2)M_i^2} \right)} \quad (33)$$

$$M_i = \left[\frac{2}{\gamma - 1} \left(\frac{1 + \frac{\gamma - 1}{2} M_n^2}{(p_i/p_n)^{(\gamma - 1)/\gamma}} \right) \right]^{1/2} \quad (34)$$

The Newtonian model assumes that the freestream flow is a stream of particles in rectilinear motion. Upon contact with the body, this stream loses momentum normal to the body surface but retains momentum tangential to the surface. These assumptions are reasonably similar to the case where the freestream Mach number is large, i.e. hypersonic flows. Modified-Newtonian theory can be applied to blunt bodies. For blunt-nose projectiles modified-Newtonian theory can be combined with second-order shock-expansion theory to provide inviscid flow surface profiles over the entire projectile. In contrast, linearized perturbation theory can be applied solely to pointed-nose projectiles.

2. Viscous Methods

The viscous flowfield is considered to be limited to projectile surface boundary layers. For steady two-dimensional/axisymmetric flow, the governing boundary-layer equations describe the conservation of mass, momentum, and energy in a compressible flow.

$$\frac{\partial(r^k \bar{p} \bar{u})}{\partial x} + \frac{\partial(r^k \bar{p} \bar{v})}{\partial y} = 0 \quad (35)$$

$$\bar{p} \bar{u} \frac{\partial \bar{u}}{\partial x} + \bar{p} \bar{v} \frac{\partial \bar{u}}{\partial y} = - \frac{d \bar{p}}{dx} + \frac{1}{r^k} \frac{\partial}{\partial y} \left[r^k \left(\bar{u} \frac{\partial \bar{u}}{\partial y} - \bar{p} \bar{u}' \bar{v}' \right) \right] \quad (36)$$

⁴⁸ Anderson, J.D., *Hypersonic and High Temperature Gas Dynamics*, McGraw-Hill, 1989.

$$\bar{\rho u} \frac{\partial \bar{H}}{\partial x} + \bar{\rho v} \frac{\partial \bar{H}}{\partial y} = \frac{1}{r^k} \frac{\partial}{\partial y} \left[r^k \left\{ \mu \left(1 - \frac{1}{\text{Pr}} \right) \bar{u} \frac{\partial \bar{u}}{\partial y} + \frac{\bar{\mu}}{\text{Pr}} \frac{\partial \bar{h}}{\partial y} - \bar{\rho} \bar{v}' \bar{h}' \right\} \right] \quad (37)$$

where k is 1 for axisymmetric flow and 0 for two-dimensional flow.

The boundary conditions for Equations 35-37 are prescribed as zero velocity on the walls and $\lim_{y \rightarrow y_e} \bar{u}(x, y) = \bar{u}_e(x)$, $\lim_{y \rightarrow y_e} \bar{h}(x, y) = \bar{h}_e(x)$ at the boundary layer edge. The boundary layer edge velocity and enthalpy, u_e and h_e , are prescribed as well. The reference velocity is the freestream value, V_∞ . The coordinate x denotes the distance along the surface measured from the stagnation point or the leading edge of the body. The coordinate y is measured normal to the body surface, which is at a radius of r from the body centerline. The equations are written for turbulent boundary layer flow and thus the overbar (\bar{u}) represents a time-averaged quantity and the turbulent transport properties are represented by $-\bar{\rho} \bar{u}' \bar{v}'$ and $-\bar{\rho} \bar{v}' \bar{h}'$. Closure assumptions must be made for these terms. The Boussineq eddy-diffusivity concept⁴⁹ is used for that purpose.

$$-\bar{\rho} \bar{u}' \bar{v}' = \bar{\rho} \epsilon_m (\partial \bar{u} / \partial y) \quad (38)$$

$$-\bar{\rho} \bar{v}' \bar{h}' = \bar{\rho} (\epsilon_m / \text{Pr}_{tr}) (\partial \bar{h} / \partial y) \quad (39)$$

The eddy viscosity, ϵ_m , is defined in terms of an inner and an outer region within the boundary layer and is based on the mixing length, L_m , concept.⁵⁰ The concept does not apply within the sublayer, therefore the calculation is started at a small distance from the wall, y_c . An intermittency term, ω_{tr} , is often introduced such that, $\omega_{tr} = 0$ for fully laminar flows, 1 for fully turbulent flows, and a function of x for transitional flows. Transitional flows are not considered here. The turbulent Prandtl number, Pr_{tr} , is a constant .9 throughout the boundary layer which is a good mean value for air.

$$(\epsilon_m)_{\text{inner}} = L_m^2 r \left| \frac{\partial u}{\partial y} \right| \omega_{tr} \quad \text{for } 0 \leq y \leq y_c \quad (40)$$

$$(\epsilon_m)_{\text{outer}} = a u_e \left| \delta^* \right| \omega_{tr} \quad \text{for } y_c \leq y \leq y_e \quad (41)$$

where,

$$a = .0168$$

$$\delta^* = \int_0^\infty (1 - (\rho u) / (\rho_e u_e)) dy$$

$$L_m = \chi y [1 - \exp(-y/\Gamma)]$$

$$\chi = .4, \text{ the von Karman constant}$$

$$\Gamma = \text{Van Driest damping length constant}$$

For continuous boundary-layer profiles, $(\epsilon_m)_{\text{inner}}$ is applied until $(\epsilon_m)_{\text{inner}} y_c = (\epsilon_m)_{\text{outer}}$. Cebeci⁴⁹⁻⁵⁰ generalized the definition of the Van Driest damping length constant, Γ , to compressible boundary-layer flows with pressure gradients, heat and mass transfer.

$$\Gamma = \Gamma^+ \left(\frac{\mu}{N} \right) \left(\frac{\tau_w}{\rho_w} \right)^{-1/2} \left(\frac{\rho}{\rho_w} \right)^{1/2} \quad (42)$$

⁴⁹ Cebeci, T., and Smith, A.M.O., *Analysis of Turbulent Boundary Layers*, Academic Press, 1974.

⁵⁰ Bradshaw, P., Cebeci, T., and Whitelaw, J.H., *Engineering Calculation Methods for Turbulent Flow*, Academic Press, 1981.

where,

$$N = [1 - 11.8(\mu_w/\mu_e)(\rho_e/\rho_w)^2 p^+]^{1/2}$$

$$p^+ = (\mu_e u_e)/(\rho_e u_r^3) \quad du_e/dx$$

$$u_r = (\tau_w/\rho_w)^{1/2}$$

Γ^+ = empirical constant which can be expressed as a function of Reynolds number.

Equations 35-37 apply to attached laminar and turbulent boundary-layer flows. Efforts to solve Equations 35-37 with flow separation (i.e. negative wall shear) are complicated both by the need to account for downstream conditions after separation and by an apparent singularity at the separation point. There is considerable analytical and numerical evidence that such a singularity exists when the steady boundary-layer equations are solved in the conventional manner with a specified boundary layer edge velocity or pressure distribution. The separation singularity has been discussed, for example by Brown and Stewartson.⁵¹ Numerical integration of the boundary-layer equations past the point of flow separation gives rise to an instability in the computation. To continue the solution downstream, it is therefore necessary to impose an asymptotic boundary condition of some kind (usually for the pressure) as $x \rightarrow \infty$.⁵² A stable, but approximate, downstream solution can be obtained without such a boundary condition using the FLARE technique first proposed by Flugge-Lotz And REyhner;⁵³ They neglect the $\bar{\rho} \bar{u} (\partial \bar{u} / \partial x)$ term in Equation 36, which is the cause of the instability, whenever $\bar{u} < 0$. Williams⁵⁴ used the FLARE approximation in an iterative solution procedure called DUIT. This procedure solved the boundary-layer equations using both a standard and an inverse method (see Section III.2.b) and links these solutions together by an iteration method. The FLARE approximation, used with a standard solution of the boundary-layer equations, accurately predicts the pressure at the boundary layer edge, but not the skin friction. However, Cebeci⁵⁵ and Carter⁵⁶ have shown that iterative procedures employing FLARE can accurately predict the skin friction. FLARE approximations have also been investigated by Kaufman⁵⁷ and McDonald and Briley.⁵⁸ In the present model, the FLARE approximation is employed in both standard and inverse boundary-layer solutions as

$$\bar{\rho} \bar{u} \frac{\partial \bar{u}}{\partial x} = C \bar{\rho} |\bar{u}| \frac{\partial \bar{u}}{\partial x}, \quad C = 1.0 \text{ when } \bar{u} > 0 \text{ and } C \leq 0.2 \text{ when } \bar{u} < 0 \quad (43)$$

Despite the utility of the FLARE approximation, the belief that the boundary-layer equations should nevertheless describe thin separation bubbles persists.⁵⁹ This idea has led naturally to the hypothesis that the singularity results from a failure to allow in some

⁵¹ Brown, S.N., and Stewartson, K., "Laminar Separation," *Annual Review of Fluid Mechanics*, Vol. 1, 1969.

⁵² Stewartson, K., and Williams, P.G., *Mathematika*, Vol. 20, 1973, pp. 98-108.

⁵³ Flugge-Lotz, I., and Reyhner, T.A., "The Interaction of a Shock Wave with a Laminar Boundary Layer" *International Journal of Non-Linear Mechanics*, Vol. 3, 1968, pp. 173-199.

⁵⁴ Williams, P.G., "A Reverse Flow Computation In The Theory of Self-Induced Separation," *Lecture Notes in Physics*, Vol. 38, *Proceedings of the 4th International Conference on Numerical Methods in Fluid Dynamics*, Springer-Verlag, 1978.

⁵⁵ Cebeci, T., "Separated Flows and Their Representation by Boundary Layer Equations," *Report ONR-CR 215-234-2*, Office of Naval Research, Arlington, VA, 1976.

⁵⁶ Carter, J.E., "A New Boundary-Layer Interaction Technique for Separated Flows," *NASA TM-78690*, June 1978.

⁵⁷ Kaufmann, K.C., and Hoffman, G.H., "A Unified Approach to Direct and Inverse Boundary Layer Solutions," *International Journal for Numerical Methods in Fluids*, Vol. 8, 1988, pp. 1367-1388.

⁵⁸ McDonald, H., and Briley, W.R., "A Survey of Recent Work on Interacting Boundary-Layer Theory for Flow With Separation," *Numerical and Physical Aspects of Aerodynamic Flows II*, (Cebeci, ed.) Springer-Verlag, 1984.

⁵⁹ Briley, W.R., and McDonald, H., "Numerical Prediction of Incompressible Separation Bubbles," *Journal of Fluid Dynamics*, Vol. 69, Pt. 4, 1975, pp. 631-656.

manner for interaction with the inviscid flow. Since the usual singularity is manifested by an infinite boundary layer displacement thickness and an infinite streamwise gradient of the wall shear at separation, efforts have been made to compute inverse solutions to the boundary-layer equations by specifying a smooth displacement thickness and computing the resultant velocity distribution. There is extensive numerical evidence that this procedure removes the singularity at separation.

Equations 35-37 can be solved in a standard or inverse procedure, with each having particular applications and advantages. In the standard solution, the pressure gradient ($d\bar{p}/dx$) imposed upon the boundary layer by the inviscid flowfield is specified. The numerical integration of the equations then yields $\bar{u}(x, y)$, $\bar{v}(x, y)$, $\bar{h}(x, y)$, $\bar{p}(x, y)$, δ^* , and $C_f = 2\tau_w/(\bar{\rho}u_\infty^2)$ where $\tau_w = \mu\partial\bar{u}/\partial y$. In the inverse solution, the boundary layer displacement thickness, δ^* , or skin friction, C_f , distribution is specified. The numerical integration of the equations then yields $\bar{u}(x, y)$, $\bar{v}(x, y)$, $\bar{h}(x, y)$, $\bar{p}(x, y)$, and p_e or u_e distributions. The boundary layer edge pressure and velocity are related by, $-dp/dx = \rho_e u_e du_e/dx$, (Euler's equation).

a. Standard Solution Procedure

The boundary-layer equations can be numerically integrated using the CS method by Cebeci and Smith.⁴⁹ In the CS method, Equations 35-37 are transformed into nearly two-dimensional form using the Mangler transformation and the Levy-Lees transformation in order to remove the singularity at $x = 0$ and stretch the coordinates in the x and y directions. The combined Mangler-Levy-Lees transformation is given by

$$d\xi = \rho_e \mu_e u_e [r(x)/L_r]^{2k} dx \quad \text{and} \quad d\eta = [\rho u_e / (2\xi)^{1/2}] [r(x)/L_r]^k dy \quad (44)$$

where L_r is a reference length. The stream function, ψ , is defined in terms of \bar{p} , \bar{u} , and \bar{v} . A dimensionless stream function, f , is related to ψ as follows:

$$\psi(x, y) = (2\xi)^{1/2} L_r^k f(\xi, \eta) \quad \text{where} \quad \frac{\partial\psi}{\partial y} = r^k \bar{p} \bar{u}, \quad -\frac{\partial\psi}{\partial x} = r^k \bar{p} \bar{v} \quad (45)$$

Equation 35 is automatically satisfied by the definition of ψ . Equations 36 and 37 become the transformed momentum and energy equations for two-dimensional and axisymmetric laminar and turbulent boundary layers. For convenience the overbar, (\bar{u}), notation has been dropped.

$$(bf'')' + ff'' + \lambda[c - (f')^2] = 2\xi \left(f' \frac{\partial f'}{\partial \xi} - f'' \frac{\partial f}{\partial \xi} \right) \quad (46)$$

$$(a_1 g' + a_2 f' f'')' + fg' = 2\xi \left(f' \frac{\partial g}{\partial \xi} - g' \frac{\partial f}{\partial \xi} \right) \quad (47)$$

where,

$$()' = \partial/\partial\eta$$

$$f' \equiv u/u_e$$

$$b = (1 + \tau)^{2k} K(1 + \epsilon_m^+)$$

$$K = \rho\mu/\rho_e\mu_e$$

$$\begin{aligned}
\epsilon_m^+ &= \rho \epsilon_m / \mu \\
\lambda &= (2\xi/u_e)(du_e/d\xi) \\
c &= \rho_e / \rho \\
g &= h/h_e \\
a_1 &= (1+\tau)^{2k} (K/\text{Pr}) [1 + \epsilon_m^+ (\text{Pr}/\text{Pr}_t)] \\
a_2 &= (1+\tau)^{2k} K (u_e^2/h_e) [1 - (1/\text{Pr})] \\
\tau &= \text{the transverse curvature parameter, 0 for zero yaw}
\end{aligned}$$

The boundary conditions and eddy viscosity formulae are also transformed. Equations 46 and 47, for a given pressure gradient parameter λ , contain only derivatives in the body-normal direction, η . The equations can therefore be solved using a marching technique from an initial solution at $\xi = 0$ to any location downstream on the body. It is exactly this characteristic that leads to the instability for separated flows, discussed above, and for which the FLARE approximation is applied to the $f' \partial f' / \partial \xi$ term in Equation 46. The initial solution (at $\xi = 0$) can be obtained from the compressible similar boundary-layer equations for which solutions are well known.⁴⁹

The CS method uses the Keller Box Scheme to numerically integrate Equations 46 and 47. The scheme is accurate and efficient for solving laminar and turbulent boundary-layer equations. The scheme was developed by Keller,⁶⁰ and the application to boundary-layer equations was given by Cebeci and Smith.⁴⁹ One of the basic features of the scheme is to write the governing system of partial differential equations in the form of a first-order system. Thus derivatives of some quantities with respect to the normal variable, η , must be introduced as new unknown functions. Derivatives with respect to all other (streamwise) variables occur only to first order, as a consequence of the boundary-layer approximations. With the resulting first-order system and the use of an arbitrary rectangular grid, centered-difference quotients and averages at the midpoints of the grid cells yield second-order accurate finite-difference equations. The scheme is unconditionally stable, but the equations are implicit and highly nonlinear. Newton's method is used as a solution technique along with block-tridiagonal factorization.

b. Inverse Solution Procedure

Inverse solution of Equations 46 and 47 has been shown to be useful in the numerical integration of the boundary-layer equations past the point of vanishing wall shear stress (i.e. separated flow) by Cebeci.⁶¹ In the inverse solution procedure, the boundary layer displacement thickness, δ^* , or skin friction, C_f , distribution is specified.

$$\delta^* = \int_0^\infty \left(1 - \frac{\bar{\rho}u}{\bar{\rho}_e u_e} \right) dy \quad (48)$$

$$C_f = \frac{2\tau_w}{\bar{\rho}u_\infty^2} \quad (49)$$

⁶⁰ Keller, H.B., "A New Difference Scheme for Parabolic Problems," *Numerical Solutions of Partial Differential Equations II*, (Bramble ed.) Academic Press, 1970.

⁶¹ Cebeci, T., "An Inverse Boundary-Layer Method for Compressible Laminar and Turbulent Boundary Layers," *AIAA Journal of Aircraft*, Vol. 13, No. 9, Sept. 1976, pp. 709-717.

The numerical integration of the boundary-layer equations then yields the boundary layer profiles as well as the edge velocity (from which the edge pressure can be computed using Euler's equation, Equation 4).

To describe the inverse solution procedure of Cebeci, assume (or solve for using the standard solution procedure) the quantities $f, f', f'', g, g', \lambda$, and u_e at $x = x_{i-1}$. At $x = x_i$ the solution of Equations 46 and 47 for a given δ^* is required. To start the calculation it is necessary to know $\lambda(x_i)$ and $u_e(x_i)$. A value of $\lambda(x_i)$ is chosen (possibly extrapolated from upstream values), and a value for $u_e(x_i)$ is calculated from the definition of λ . Using a central finite-difference for $\lambda(x_{i-1/2})$ in terms of $\lambda(x_i)$ and $\lambda(x_{i-1})$, $u_e(x_i)$ is determined obtained using

$$u_e(x_i) = -u_e(x_{i-1}) \frac{\lambda(x_{i-1/2}) + 2\omega_i}{\lambda(x_{i-1/2}) - 2\omega_i} \quad (50)$$

where $\omega_i = x_{i-1/2}/[x_i - x_{i-1}]$ and $\lambda(x_{i-1/2}) = [\lambda(x_i) - \lambda(x_{i-1})]/2$

Once $\lambda(x_i)$ and $u_e(x_i)$ are known, then the standard solution procedure can be used to solve for the boundary layer profiles and δ^* (denoted δ_s^*) at $x = x_i$. Recall that the desired value for the displacement thickness is δ^* . The function π is then formed:

$$\pi[\lambda(x_i)] = \delta_s^* - \delta^* \quad (51)$$

$\lambda(x_i)$ is determined such that $\pi[\lambda(x_i)] = 0$. This rootfinding problem can be efficiently solved using the secant method.⁶² For two initial guesses, $\lambda^0(x_i)$ and $\lambda^1(x_i)$, an iteration procedure can be formed such that

$$\lambda^{i+1}(x_i) = \lambda^i(x_i) \frac{\pi[\lambda^i(x_i)]}{\pi[\lambda^i(x_i)] - \pi[\lambda^{i-1}(x_i)]} (\lambda^i(x_i) - \lambda^{i-1}(x_i)) \quad (52)$$

Equation 52 converges rapidly for most applications and yields the values of $\lambda(x_i)$ and thus $u_e(x_i)$ for the specified value of the displacement thickness, $\delta^*(x_i)$. The same procedure can be used for a specified C_f .

Cebeci⁶³ has shown that the inverse solution procedure yields good results for nearly-separated (i.e. negligible wall shear) and separated (i.e. negative wall shear) flows, when compared to data measured for decelerating flows and flows with strong adverse pressure gradients. In some cases the inverse solution method yielded results that were superior when compared to those of the standard solution method.

Carter⁶⁴ has employed an inverse approach for an incompressible boundary-layer solution using a different iteration procedure than described above. This approach is adequate for solving two-dimensional, as well as three-dimensional, laminar boundary layers that were undergoing separation and reattachment.⁶⁵

⁶²Anderson, D.A., Tannehill, J.C., and Pletcher, R.H., *Computational Fluid Dynamics and Heat Transfer*, Hemisphere Publishing Corp., McGraw-Hill, 1984.

⁶³Cebeci, T., Khalil, E.E., and Whitelaw, J.H., "Calculation of Separated Boundary-Layer Flows," *AIAA Journal*, Vol. 17, No. 12, Dec. 1979, pp. 1291-1292.

⁶⁴Carter, J.E., "Inverse Solutions For Laminar Boundary-Layer Flows With Separation and Reattachment," *NASA TR R-447*, Nov. 1975.

⁶⁵Edwards, D.E., Carter, J.E., and Smith, F.T., "Analysis of Three-Dimensional Separated Flow with the Boundary-Layer Equations," *AIAA Journal*, Vol. 25, No. 3, March 1987, pp. 380-387.

3. Interaction Method

For aerodynamic design calculations it is common to obtain the pressure distribution about a body using an inviscid flowfield solution. The inviscid solution provides the necessary boundary condition for solving the boundary-layer equations. For large freestream Reynolds numbers and smooth body geometries, the presence of the viscous boundary layer only slightly modifies the inviscid flow over the body. An improved inviscid flow solution can be obtained by augmenting the physical profile of the body with the boundary layer displacement thickness. The improved inviscid edge velocity distribution can then be used to obtain yet another viscous flow solution. In principle, this viscous-inviscid interaction procedure can be continued in an iterative fashion until the pressure distribution about the body converges. In practice, however, severe underrelaxation of the changes from one iterative cycle to another is often required to achieve convergence.⁶² For high Reynolds number flows, where the boundary layer is attached, the improvement in solution accuracy gained from viscous-inviscid interaction is negligibly small. In these cases it suffices for engineering design purposes to compute the inviscid and viscous flows independently, in order to determine the pressure and skin friction drag, respectively. Flows which separate or contain separation bubbles are a notable exception. The displacement effect caused by the separated regions of the flow locally alter the pressure distribution in a significant manner. A rapid thickening of the boundary layer under the influence of an adverse pressure gradient (e.g. near a flared afterbody), even without separation, can also alter the pressure distribution to an extent that a reasonable solution cannot be achieved without viscous-inviscid interaction. Indeed, without accounting for displacement effects, the solution obtained may predict flow separation when the flow does not separate at all.

The essential elements of a viscous-inviscid interaction calculation procedure are: 1) a method for obtaining the inviscid flowfield about a body of arbitrary cross section in order to account for viscous flow displacement effects, 2) a technique for obtaining a solution to the boundary-layer equations suitable for the problem at hand – an inverse boundary-layer procedure would be appropriate for a flow which may separate, and 3) a procedure for relating the inviscid and viscous flow solutions in a manner which will drive the changes from one iteration cycle to the next toward zero. The techniques required for items 1 and 2 have been described in the previous sections. The interaction procedure is described in this section.

A number of viscous-inviscid interaction schemes have been proposed. Briley and McDonald⁵⁹ used a time-dependent interaction scheme for incompressible flows with thin separation bubbles. They also surveyed a wide range of interaction schemes. Carter⁵⁶ developed an interaction scheme for transonic and supersonic separated flows that was used for incompressible separated flows by Kwon and Pletcher.²⁸ This latter scheme is employed in the present model.

The interaction calculation proceeds in the following way. First, the inviscid edge velocity and the boundary layer flow are computed up to the beginning of the specified interaction region ($x = x_1$). A standard solution to the boundary-layer equations is employed. These two solutions do not change. Next, an initial boundary layer displacement thickness, $\delta^*(x)$, distribution is chosen over the interaction region, $x_1 < x < x_2$. This

initial guess is purely arbitrary, but it should match the $\delta^*(x)$ computed by the standard method at $x = x_1$. The boundary-layer solution is obtained by an inverse method using this $\delta^*(x)$ as a boundary condition, yielding the edge velocity distribution, $u_{e,bl}(x)$. Now the inviscid solution is used to obtain $u_{e,inv}(x)$ using the body profile augmented by the displacement thickness, $\delta^*(x)$. The $u_e(x)$ from the two calculations, boundary-layer and inviscid, will not agree until convergence has been achieved.

The difference between $u_e(x)$ calculated for inviscid and boundary-layer flows can be used as a potential to calculate an improved distribution for $\delta^*(x)$. A suitable scheme follows from the observation that the volume flow rate per unit width in the boundary layer tends to be preserved, i.e. $u_e \delta^* \simeq \text{constant}$. This implies that a local decrease in $u_e(x)$ (associated with a more adverse pressure gradient) causes an increase in $\delta^*(x)$ and a local increase in $u_e(x)$ (associated with a more favorable pressure gradient) causes a decrease in $\delta^*(x)$. This concept is used to compute the new distribution of $\delta^*(x)$ using

$$(\delta^*)^{i+1} = (\delta^*)^i \left(\frac{u_{e,bl}^i}{u_{e,inv}^i} \right) \quad (53)$$

where i denotes the iteration level. At convergence $u_{e,bl} = u_{e,inv}$; thus Equation 53 represents an identity thereby having no effect on the final solution. Equation 53 only serves as a basis for correcting δ^* between iterative passes. No formal justification for the use of Equation 53 is required so long as the iterative process converges. However, Carter⁶⁴ has derived a formal justification of Equation 53 based on the von Karman momentum integral for boundary-layer flows. Kwon and Pletcher²⁸ have found that convergence can be accelerated by augmenting Equation 53 with successive over-relaxation (SOR):

$$(\delta^*)^{i+1} = \text{RF} \left[(\delta^*)^i \left(\frac{u_{e,bl}^i}{u_{e,inv}^i} \right) \right] + (1 - \text{RF}) (\delta^*)^i \quad (54)$$

where RF is the relaxation parameter. Kwon and Pletcher²⁸ found that $1.2 \leq \text{RF} \leq 1.8$ produced adequate convergence acceleration.

The viscous-inviscid interaction procedure is completed by making successive passes first through the inverse boundary-layer scheme, then through the inviscid flow scheme with δ^* being computed by Equation 53 and 54 prior to each boundary-layer calculation. Convergence is said to have occurred when

$$\frac{|u_{e,bl} - u_{e,inv}|}{u_{e,inv}} \leq \text{the prescribed tolerance} \quad (55)$$

4. Small Yaw Procedure

The calculation of the surface pressures on a body of revolution is considerably more complicated when the body is inclined to the flow. When the body is not inclined, the meridian lines on the surface are coincident with the streamlines, and the analysis used for the nonlifting body is adequate. At incidence, the streamlines deviate considerably from the meridian lines because of the crossflow component of the flow on the surface. If the shape of the streamlines can be approximated and this shape used to generate a body

of revolution, it is reasonable to assume that the analysis for the nonlifting body can be used to provide the pressure variation along a meridian of this body of revolution and, therefore, along the streamline itself.

The approach taken in this report, after Jackson et.al.,⁶⁶ is to obtain the coordinates of the streamlines in the vertical plane ($\phi = 90^\circ$) for the body of revolution at angle of attack, α , by transforming the body-axis coordinates (x, y) into the wind-axis coordinates ($x_{\text{wind}}, y_{\text{wind}}$). In the wind-axis system, the circumferential angle, ϕ , is transformed to Ω where $\phi = 0^\circ$ and $\Omega = -90^\circ$ correspond to the windward side and where $\phi = 180^\circ$ and $\Omega = +90^\circ$ correspond to the leeward side; thus $\Omega = \phi - 90^\circ$. This transformation results in a rotation of the coordinate system. If the body has a blunt nose cap of radius r_n , the center of rotation is taken to be the center of the cap. The streamline for $\Omega = 0^\circ$ is approximated by the body-axis coordinates of a meridian for the true body shape. These assumptions imply that the coordinates of the streamlines on the body at angle of attack vary from body-axis coordinates at $\Omega = 0^\circ$ to wind-axis coordinates at $\Omega = \pm 90^\circ$. This variation is represented for $-90^\circ \leq \Omega \leq 90^\circ$ by the expressions:

$$x_{\text{wind}} = \left(\frac{r_n(\cos\alpha - 1) + x + (y\cos\alpha - (x - r_n)\sin\alpha)\sin\alpha}{\cos\alpha} - x \right) \sin\Omega + x \quad (56)$$

$$y_{\text{wind}} = (y\cos\alpha - (x - r_n)\sin\alpha - y)\sin\Omega + y \quad (57)$$

Using Equations 56 and 57, the coordinates of the streamlines in the wind-axis system are obtained, and these coordinates are used to generate bodies of revolution for each circumferential angle, Ω , of interest. Estimates of pressure distribution along the body-axis meridians are obtained by applying the analysis used for the nonlifting body to equivalent bodies generated from the streamlines. The use of this concept involves two basic limitations: (1) the angle of attack, α , is small enough for the stagnation point to remain on the nose cap (if the body is blunt) and (2) the angle of attack is small enough for the coordinates of the equivalent body for $\Omega = 90^\circ$ (leeward side) to remain positive.

Such a system of transformations result in engineering estimates of the streamline shape as well as the pressure variation along the meridians. An examination of these transformations (Equations 56 and 57) shows the incidence approaches zero ($\alpha \rightarrow 0^\circ$) as the approximate streamline shapes approach the body meridian shapes (i.e. true streamline shapes at $\Omega = 0^\circ, \phi = 90^\circ$). This approach should, therefore, be valid for the case where the body incidence is small and crossflow on the projectile is negligible.

IV. HEAT TRANSFER ANALYSIS

Hypersonic projectiles which attain speeds of 2 to 3 km/s at sea level (Mach number 6 to 9) are exposed to extreme thermal and aerodynamic loads. The stagnation point heat flux can exceed 10 kW/cm² while stagnation pressures range from 40 to 100 atms. These

⁶⁶ Jackson, C.M., Sawyer, W.C., and Smith, R.S., "A Method For Determining Surface Pressures on Blunt Bodies of Revolution at Small Angles of Attack in Supersonic Flow," NASA TN D-4865, November 1968.

instantaneous loads can be considerably larger than those encountered by reentry vehicles. However, the residence time in this environment is much less than the corresponding time of maximum aerobraking of reentry vehicles. Consequently, an accurate prediction of the thermal loads is crucial in determining an optimal configuration and material for hypervelocity projectiles. A poorly conceived design could result in substantial material loss and projectile deceleration. This subsequent degradation in kinetic energy could defeat the purpose of the design. Overall, the design objective is to simultaneously reduce the aerodynamic drag and the surface heat flux.

In general, the aerothermodynamic environment is strongly dependent upon the projectile shape, Mach number, and the Reynolds number (and Knudsen number for high-altitude flight). The surface temperature of the projectile, which also effects the flowfield, is a function of the surface heat flux, geometry, and physical properties. Certain structural effects result from this rapid transient heating. In a precise analysis, the heating and structural problems are coupled, and it is only with certain approximations that the two can be treated separately. In this report structural heat conduction is not addressed. The aerodynamic heat transfer to the projectile surface is calculated assuming a constant projectile wall surface temperature.

Computational procedures for aerothermodynamic prediction of high-speed projectiles may be categorized as: reliable semi-empirical methods based on benchmark solutions and experimental data or advanced numerical schemes (e.g. real-gas CFD codes) for the solution of the entire flowfield. The approximate methods yield results with only a fraction of the computational time required for the numerical schemes. In addition, the code development based on these approximate methods is straightforward, while the numerical schemes usually require substantial code development, input setup, and grid generation. Approximate algebraic equations have been developed which accurately predict stagnation point and laminar or turbulent heat transfer distributions for axisymmetric bodies. These equations assume that the flowfield is a continuum and chemical nonequilibrium effects are insignificant. Projectiles usually achieve significant heating rates at sufficiently low altitudes where these assumptions are reasonable. When the geometry and the subsequent flowfield are more complicated, the numerical schemes will be required.

Before presenting the formulae for heat transfer prediction used in this report it is appropriate to review some basic tenets of aerodynamic heat transfer. The phenomenon of heat transfer between a flowing fluid and a body immersed in the fluid is a classical engineering problem. For the purposes of this analysis aerodynamic heating is defined as the heating of a body due to the high speed flow of a gas over the body, including negative heating (cooling), of the body. The basic principles of aerodynamic heating are contained in boundary layer theory. In the boundary layer, kinetic energy is transformed into thermal energy by frictional forces and compression forces. The temperature of the gas in the thin boundary layer is raised, and the amount of heat transferred is proportional to the difference between the body surface temperature and some representative temperature, T_r , of the hot gas. Denoting \dot{q}_w as the heat transfer to the wall per unit area and per unit time from a fluid of temperature T_r to a body of surface temperature T_w , then Newton's law relates \dot{q}_w to a heat transfer coefficient, C_h , as

$$\dot{q}_w = C_h(T_r - T_w) \quad (58)$$

The gas temperature T_r is called the recovery temperature and is defined from the freestream temperature, Mach number, Prandtl number, and ratio of specific heats using⁴²

$$T_r = T_\infty + \text{Pr} \left(\frac{V_\infty^2}{2c_p} \right) = T_\infty \left(1 + \text{Pr} \left(\frac{\gamma - 1}{2} \right) M_\infty^2 \right) \quad (59)$$

At the stagnation point on the body, $\text{Pr} = 1$, and the recovery temperature is equivalent to the total temperature, T_t , of the fluid. The determination of C_h and thus \dot{q}_w is complicated due to the dependence on T_w . In general, the wall temperature is based on solving heat conduction equations within the body based on values of \dot{q}_w as input. However, \dot{q}_w depends on T_w . Thus, the heat conduction equation, which is linear, has a nonlinear boundary condition. However, the dependence of \dot{q}_w on T_w/T_r is not very strong³¹. Thus, for a first approximation, \dot{q}_w may be considered to be independent of T_w (or $T_w = \text{constant}$) for short time of flight simulations. More accurate results could be achieved using a heat transfer/conduction interaction method.

In this report, separate algebraic formulae are used to compute the heat transfer rates at the projectile stagnation point and along the projectile surface for laminar and turbulent boundary layers. The boundary layer properties required for these formulae are computed using the INTERACT code described in section III.

Heat transfer rates at the stagnation point on a blunt-nose projectile are calculated using correlation formulae for a gas in chemical equilibrium. These formulae are given by Fancett³⁸ based on the work of Fay and Kemp.³⁶ In this formula the stagnation point heat transfer rate, \dot{q}_n in kW/m^2 , is computed from the freestream velocity, V_∞ in m/s , the normal shock stagnation pressure, $(p_t)_n$ in atm , and the blunt-nose radius, r_n in cm . The expression is formally valid for a constant projectile wall temperature of 300K.

$$\dot{q}_n = 2.428 \times 10^{-4} \ (V_\infty)^{2.1085} \ ((p_t)_n/r_n)^{1/2} \quad (60)$$

$$\text{where, } (p_t)_n = \frac{2\gamma M_\infty^2 - (\gamma - 1)}{\gamma + 1}$$

Rubesin and Johnson³³ and Young and Janssen³⁴ have shown that if the values of the density and viscosity in a boundary layer are calculated with relationships which hold for constant property fluids at an intermediate "reference enthalpy", defined by an empirical expression, then they accurately describe the actual conditions in a supersonic boundary layer. Eckert³⁵ used this "reference enthalpy" technique to calculate heat transfer rates in a zero pressure gradient flow. He used the empirical expression for "reference enthalpy" temperature, T^* , suggested by Young and Janssen³⁴ which involves the body wall (T_w), freestream (T_∞), and the recovery (T_r) temperatures in Kelvin.

$$T^* = T_\infty + \frac{T_w - T_\infty}{2} + .22(T_r - T_\infty) \quad (61)$$

Fancett³⁸ derived an expression for the laminar and turbulent heating rate distributions over a wall, \dot{q}_w in W/m^2 , using these techniques. For a laminar boundary layer:

$$\dot{q}_w = 3.32 \ \frac{(\text{Re}_\sigma^*)^{1/2}}{\sigma} \ \mu^* \ (\text{Pr}^*)^{-2/3} \ c_p \ (T_r - T_w) \quad (62)$$

For a turbulent boundary layer:

$$\dot{q}_w = 1.76 (\log_{10} \text{Re}_\sigma^*)^{-2.45} c_p \mu^* \frac{\text{Re}_\sigma^*}{\sigma} (T_r - T_w) \quad (63)$$

where σ is the body surface distance from the stagnation point in m, c_p is the specific heat at constant pressure in J/(kg·K) for air at freestream conditions, μ^* is the local viscosity in kg/(m·s) based on Sutherland's law and T^* , Re_σ^* is the local Reynolds number based on the local density, viscosity (using T^*), and σ , and Pr^* is the local Prandtl number based on μ^* and c_p .

The specific heat at constant pressure used in Equations 62 and 63 can be formulated to include real gas effects in the form of a temperature dependence.⁴² For a diatomic gas, such as O_2 :

$$c_p = \frac{7}{2} \mathfrak{R} + \mathfrak{R} \left(\frac{\theta_v/2T}{\sinh(\theta_v/2T)} \right)^2 \quad (64)$$

where, $\theta_v = 2230\text{K}$ for O_2 , T is the gas temperature in K, and \mathfrak{R} is the specific gas constant in J/kg·K. Note, for $T \ll \theta_v$, $c_p \rightarrow (7/2)\mathfrak{R}$, and $T \gg \theta_v$, $c_p \rightarrow (9/2)\mathfrak{R}$.

The Stanton number distribution over the projectile surface is computed from the heat transfer rate distribution. The Stanton number based on boundary layer edge conditions and Stanton number based on freestream conditions are defined as

$$\text{St}_e = \frac{\dot{q}_w}{\rho_e u_e c_p (T_r - T_w)} \quad (65)$$

$$\text{St}_\infty = \text{St}_e \frac{\rho_e u_e}{\rho_\infty u_\infty} \quad (66)$$

V. CODE VALIDATION

1. Flow Profiles

In this section pressure coefficient distributions over projectile surfaces as predicted using the INTERACT code are compared to measurements on wind tunnel models. These models were instrumented with surface pressure taps and transducers with a reported accuracy of about 2% of the freestream pressure.⁶⁷⁻⁶⁸ Since the INTERACT code has been setup for solely axisymmetric geometries, fin-stabilized projectiles are not addressed in this report. Instead, long-rod projectiles that are flare-stabilized are considered. Preliminary design investigations for hypersonic projectiles have also considered flare-stabilization over the use of fins, primarily due to the enhanced resistance to thermal damage in flight.

Figure 4 shows the pressure coefficient distribution along a 5-degree cone, cylinder midsection, and 4-degree flare afterbody tested in a wind tunnel at Mach = 2 and a Reynolds number, based on total body length, of 7.6 million (Re based on body diameter

⁶⁷ Washington, W.D., and Humphrey, J.A., "Pressure Measurements on Four Cone-Cylinder-Flare Configurations at Supersonic Speeds," U.S. Army Missile Command Report No. RD-TM-69-11, 20 Oct. 1969.

⁶⁸ Gray, J.D., "Laminar Boundary-Layer Separation on Flared Bodies at Supersonic and Hypersonic Speeds," U.S. Air Force Systems Command AEDC-TR-64-277, Jan. 1965.

of .5 million).⁶⁷ For free flight at sea level the Re would be 15 million for $Mach = 2$. The model was at zero yaw. The cone section extends to $x/D = 5.6$, the cylinder section extends to $x/D = 14.2$, and the flare afterbody extends to the total body length of about 16.2 calibers. The numerical prediction using the INTERACT code is shown with an inviscid ($Re = \infty$) calculation. The prediction that couples the viscous effects with the inviscid flow yields the best comparison with the measured data. Note that both calculations reproduce the second-order effects over the cylinder and flare sections. Note also that the fully-coupled solution indicates a small degree of boundary-layer-induced upstream influence at the cylinder-flare junction.

Figure 5 shows the pressure coefficient distributions along the same configuration as Figure 4 but at Mach numbers of 2 and 4 (Reynolds number held constant). Both the measured data⁶⁷ and the INTERACT calculations indicate that the stabilizing effect of the flared afterbody (caused by pressure levels that are higher than the cone pressure) is reduced with increased Mach number. Agreement between the code and data is slightly better for $Mach = 2$ at a constant Re . For these wind tunnel tests⁶⁷ the Mach number is increased by increasing the supply (total) pressure (i.e. static pressure reduced), while holding the total temperature constant, thus resulting in a constant Re value. Whereas for free flight, an increase in Mach number from 2 to 4 results in an increase in Re from 15 to 30 million. This effect on the boundary-layer thickness in an adverse pressure gradient can be overpredicted by the turbulence model, especially on the flare.

Figures 6 and 7 show the pressure coefficient distributions along projectiles with 6-degree and 8-degree flare afterbodies for Mach numbers 2 thru 5 and $Re = 7.6$ million.⁶⁷ The numerical predictions using the INTERACT code reproduce pressure levels and trends well. For a flare angle of 8-degrees and Mach number 5 (Figure 7), the boundary layer over the flare thickens rapidly and reduces flare pressures. The calculations do not adequately simulate this effect. Investigation reveals that steep flare angles for low Reynolds number (less than 10 million) flows repeatedly demonstrate this effect in wind tunnel experiments. Although this effect is included in the code through the viscous-inviscid coupling (see discussion below), the magnitude of the predicted effect is smaller than measured. However, the flare pressure level at the end of the body is reproduced by the code.

This phenomena is further demonstrated in Figure 8. This figure shows the pressure distribution measured in a wind tunnel⁶⁸ along a 20-degree flare with $Re = 18$ million. Two sets of data are shown. For $M_\infty = 3$, the cylinder section of the body was shorter and thus the flare begins at $x/D = 5.8$, while the $M_\infty = 8.1$ flare begins at $x/D = 6.8$. The flares for both models are of equal length. This geometry represents a severe test of the INTERACT code, since a flare angle of this magnitude causes rapid boundary layer thickening immediately after the cylinder-flare junction. This effect may not be reproducible using the current turbulence model. However, as an illustration of the viscous-inviscid coupling, these cases were computed. For the $M_\infty = 3$ case an Euler/boundary-layer solution and the coupled viscous-inviscid solution are compared to the measured data. The trend of reduced pressure over the inviscid result downstream of the cylinder-flare junction is modeled by the coupled solution. The overall computed pressure level on the flare is 10% smaller than measured. This is produced by the cylinder flow that is not fully recompressed (i.e. $C_p < 0$) at the flare junction, as required by the second-order shock-expansion inviscid theory (section III.1.b). For the $M_\infty = 8.1$ case, the coupled INTERACT solution

compares well with the measured data. Again, the magnitude of the initial pressure level reduction is overpredicted, but the overall flare pressure is reproduced. The cylinder flow for this case was nearly recompressed (i.e. $C_p \simeq 0$) as required by the theory.

Figure 9 shows the pressure coefficient distribution measured for a 6-degree flared body at $Mach = 2$, $Re = 7.6$ million, and one-degree of yaw.⁶⁷ Computations using INTERACT for the windward and leeward sides ($\phi = 0^\circ, \phi = 180^\circ$) are compared to the data. Cone and cylinder section pressure levels for the windward side are slightly overpredicted and underpredicted for the leeward side. Pressure levels on the flare afterbody are reproduced by the code. Recall that the small yaw procedure used in INTERACT (section III.4) assumes no cross flow over the body. Small cross flow effects on the surface pressure are illustrated on the cone and cylinder sections. The effect of these pressure differences on the aerodynamic stability predictions is addressed in the following subsection.

Overall, the ability of the INTERACT code to reproduce body surface pressure coefficient distributions has been demonstrated. The wind tunnel measurements available for comparison were for low Re values of 7 to 18 million (relative to corresponding free flight Re values of 15 to 60 million) and in some cases steep flare angles ($\geq 6^\circ$). The trend of reduced pressure (relative to the inviscid value) downstream of the cylinder-flare junction is simulated by the viscous-inviscid interaction scheme. With increasing Mach number, reduced flare pressure levels are observed and computed. It is important to remember that these numerical simulations were performed in under one minute of CPU time on a VAX 8600 minicomputer.

2. Aerodynamic Stability

The design of projectile configurations with sufficient aerodynamic stability to sustain small-yaw flight is one of the most essential requirements of the initial design cycle. Non-spinning (or slowly rolling) projectiles must be designed to maintain static stability over the entire Mach number range in flight. Therefore, the engineering design code must reliably predict the location of the center of pressure, x_{cp} , as a function of Mach number. The INTERACT code predicts surface pressure and skin friction distributions over the projectile as a function of the circumferential body angle, ϕ , for a given M_∞ and α . The coefficients of pressure drag (C_{D_p}), normal force (C_N), and pitching moment (C_M) are then computed from integrations of surface pressure using

$$C_{D_p} = \frac{\text{Axial Force}}{q_\infty \pi D^2/4} = \frac{1}{\pi D^2/4} \int_0^L \int_0^{2\pi} C_p r \tan \delta d\phi dx \quad (67)$$

$$C_N = \frac{\text{Normal Force}}{q_\infty \pi D^2/4} = \frac{1}{\pi D^2/4} \int_0^L \int_0^{2\pi} C_p r \cos \phi d\phi dx \quad (68)$$

$$C_M = \frac{\text{Pitching Moment}}{q_\infty D \pi D^2/4} = \frac{-1}{\pi D^3/4} \int_0^L \int_0^{2\pi} C_p r x \cos \phi d\phi dx \quad (69)$$

Skin friction drag coefficient can also be computed. The moment coefficient is referenced to the nose of the projectile and is defined using pitch up as positive. The center of pressure,

also referenced to the nose of the projectile, is computed from C_N and C_M using

$$x_{cp} = \frac{-C_M}{C_N} \quad (70)$$

Center of pressure data has been measured in a wind tunnel for a 9.5°-cone, cylinder midsection, and 5°-flare configuration at Mach numbers 3 to 6.3 and small yaw.⁶⁹ The Reynolds number (based on total length) varied as a function of the Mach number between 1.2 and 6.8 million. These values of wind tunnel Re give rise to unusually thick boundary layers as observed in the test.⁶⁹ Table 2 shows the measured and computed x_{cp} values (referenced to the nose of the projectile) along with the relative errors in the predictions. The INTERACT code and the NSWC-AP code²⁰ are used to supply predictions. The codes were run with $\alpha = 1.0^\circ$ whereas the measurements were taken at an unreported angle of attack. However, center of pressure is usually insensitive to the value of α for small yaw.

Table 2. VARIATION OF CENTER OF PRESSURE WITH MACH NUMBER

Comparison made for 9.5° Cone - Cylinder - 5° Flare and $\alpha = 1.0^\circ$						
X_{cp} (cal) from the nose						
M_∞	Re (L)	Measured	NSWC Code	% error	INTERACT Code	% error
3.0	6.8×10^6	4.71	4.37	-7.2	5.21	+7.2
4.2	5.8×10^6	5.05	4.55	-9.9	5.25	+3.9
5.0	3.1×10^6	5.77	4.72	-18.2	5.30	-8.1
6.3	1.2×10^6	5.39	4.87	-9.6	5.08	-5.8
ave :			-11.2		± 6.25	

The NSWC-AP code averages 11.2% error in x_{cp} for this configuration, underpredicting the measured values. The INTERACT code averages $\pm 6.25\%$ error in x_{cp} values. The trend in measured center of pressure indicates that x_{cp} moves rearward as the Mach number increases with an shift forward on the projectile for $M_\infty = 6.3$. The forward shift is due to the decrease in Re and thickening of the boundary layer at the cylinder-flare junction thus decreasing flare effectiveness. The INTERACT code predicts the onset of this phenomena. The INTERACT code was run using linearized perturbation inviscid theory with a coupled finite-difference boundary layer solution. The NSWC-AP code uses second-order shock-expansion inviscid theory with a de-coupled empirical boundary layer solution. As noted in section III.1.a, linearized perturbation theory more closely approximates the Euler equations. Investigations using the INTERACT code reveal that the loss of flare effectiveness at Mach = 6.3 is a direct result of viscous-inviscid interaction at the cylinder-flare junction.

This analysis of predicted aerodynamic stability represents one particular projectile configuration. The INTERACT code should be checked with other wind tunnel and free

⁶⁹ Dennis, D.H., "The Effects of Boundary-Layer Separation Over Bodies of Revolution With Conical Tail Flares," NACA RM-A57130, Dec. 1957.

flight measurements of center of pressure as these data become available. The favorable comparison with measured data for a 5° flared projectile is encouraging especially since calculations were performed interactively on a VAX 8600 minicomputer.

3. Heat Transfer Profiles

In this section wall heat transfer rate, q_w , and Stanton number, St, predicted using the INTERACT code are compared to measurements on wind tunnel models. Three configurations are examined: a flat plate with sharp leading-edge, a blunt cone, and a cone-cylinder-flare. The surface heat transfer data referenced in this report, were measured on wind tunnel models using either temperature sensitive paint or surface thermocouples.³⁸

For the paint tests, the wind tunnel model is electrodeposited with copper to a thickness of .02 cm. The paint is made from materials of calibrated melting points suspended in an inert, nonflammable liquid. The paint is applied to the model and allowed to dry to a dull, opaque film. When heat is applied, the film liquefies at its temperature rating to within an accuracy of 1°C.³⁸ For the thermocouple tests the model is usually made of steel and is hollow. Thermocouples are spot welded to the inner surface of the model and the lead wires are passed out of the model thru a base seal. The air temperature inside the model is usually at the initial tunnel ambient value, which acts as an insulator to prevent heat loss from the inner surface. The thermocouples are calibrated at equilibrium when immersed in water baths of various temperatures. Paint and thermocouple tests yield the time variation of the model wall temperature, $\partial T_w / \partial t$, during the tunnel run. Local heat transfer rate is obtained from these data assuming that the diffusion time through the model wall is very small compared to the tunnel run time (about 10 sec.) and using the "thin wall" heat balance relation,³⁸

$$q_w = \rho_w c_{p_w} l_w \frac{\partial T_w}{\partial t} \quad (71)$$

where ρ_w , c_{p_w} , and l_w are the model wall density, heat capacity and thickness, respectively.

Local heat transfer rates have been measured along a flat plate 52 inches (1.32 m) in length and aligned to the freestream flow at a Mach and Reynolds number of 10.53 and 25 million (based on total length), respectively.⁷⁰ The plate wall temperature was conditioned to 4-times the freestream value before the test. Flow visualization tests indicated that boundary layer transition from laminar flow started at .23 m from the leading edge with full turbulent flow developing at .5 m. The INTERACT code is setup for both laminar and turbulent boundary layer solutions with transition specified at a discrete point. A boundary layer transition model is not included in the code. Therefore, for the flat plate calculation, transition was specified at .23 m from the leading edge.

Figure 10 shows a comparison between heat transfer rate measurements along the plate and the INTERACT code. Since the plate has a sharp leading edge, the stagnation point value is theoretically infinite. The computed laminar heating rates slightly underpredict the data. The maximum heating rate after transition to turbulent flow is reproduced

⁷⁰ Holden, M.S., "An Experimental Investigation of Turbulent Boundary Layers at High Mach Number and Reynolds Number," Cornell Aeronautical Laboratory (Calspan), Buffalo NY, Report No. AB-5072-A-1, Nov. 1972 (see also NASA CR-112147).

by the code at the specified location. The computed gradient for turbulent heating along the remainder of the plate compares well with the data. The turbulent heating level is overpredicted by the code and is probably a strong function of the turbulence model. Overall, with the exception of flow transition, the INTERACT code simulates flat plate aerodynamic heating within acceptable design accuracy. It should be noted that the hypersonic flat plate problem is not trivial since it involves strong shock-wave/boundary-layer interaction along the boundary layer edge, particularly near the plate leading edge,⁴⁸ and is a good test of the inviscid-viscous interaction scheme.

Figure 11 shows a comparison between measured and computed heat transfer rate along a 15-degree cone with a 20% nose bluntness. These data were gathered during actual high altitude ($\geq 200,000$ ft) flight tests at Mach number 10.6 and a Reynolds number of .38 million (based on total length).⁷¹ The cone wall temperature was measured at a constant value 1.76-times that of the freestream static value before data acquisition. The data have been normalized by the stagnation point heat transfer. The calculation overpredicts heat transfer along the blunt nose but reproduces the constant level of heating along the cone section of the body. For this simulation, modified-Newtonian inviscid theory and laminar boundary layer modeling were employed. The discontinuities in the otherwise smooth distribution of heat transfer are caused by rapid boundary layer growth near the stagnation point and body slope change at the cone junction ($x/D = .06$). This problem is also dominated by strong shock-wave/boundary-layer interaction. Overall, the INTERACT code predicts the heating rate to within design accuracy.

Figures 12-14 show comparisons between computed and measured Stanton number (non-dimensional heat transfer, see Equation 66) along a 5-degree blunt cone, cylinder midsection, and 5-degree flare afterbody projectile as determined in a wind tunnel by RARDE.³⁸ The freestream Mach number and Reynolds number were 5.2 and 1.7 million (based on total body length), respectively. Both zero yaw and small yaw cases were tested. Some tests were also performed for $Re = .65$ and 3.1 million. The body surface temperature was conditioned at .51-times the freestream static value of 1482 R before the tunnel was started.

Figure 12 shows that the INTERACT calculations reproduce the zero-yaw measured data very well. Heating levels on the cone, cylinder, and flare sections are predicted. Figure 13 shows a comparison between the computed and measured zero-yaw values and the transverse plane ($\phi = 90^\circ$) values at 1.25° angle-of-attack (α). Since the code does not account for cross flow, both calculated distributions are identical (see Equations 56-57). The measured data show a cross flow effect on the heating rates such that the discrepancy between measured and computed rates is $\leq 16\%$. Cross flow effects slightly increase aerodynamic heating on the flare.

Figure 14 shows a comparison between the computed and measured heating rates in the windward ($\phi = 0^\circ$) and leeward ($\phi = 180^\circ$) planes for $\alpha = 1.25^\circ$. Once again, the cross flow effects have not been accounted for in the INTERACT code. On the cone section, the measured trend of higher heat transfer on the windward side of the projectile is reproduced by the code, however the magnitude of the difference is underpredicted. On the cylinder

⁷¹ Goodrich, W.D., Li, C.P., Houston, C.K., Chiu, P.B., and Olmedo, L., "Numerical Computations of Orbiter Flowfields and Laminar Heating Rates," *AIAA Journal of Spacecraft and Rockets*, Vol. 14, No. 5, May 1977, pp. 257-264.

section, the same trend applies to the measured data. The calculation predicts a reversal in which higher heating rates occur on the leeward side at the end of the cylinder. On the flare afterbody, both measured and computed results show that heat transfer is somewhat higher on the windward side of the projectile. Flare heating rates are reproduced very well by the INTERACT code.

Table 3 shows a comparison between the computed and measured heating rate at a point on the 5-degree flare for three values of the Reynolds number. The heat transfer rate on the windward side for $\alpha = 1.25^\circ$ is normalized by the rate for zero yaw. The error in prediction is 1% to 1.5% for smaller Re and 12% for large Re values. This illustrates that cross flow effects on heat transfer on the flare become increasing important with increasing Re.

Table 3. EFFECT OF REYNOLDS NUMBER ON FLARE HEAT TRANSFER

Comparison made at X/D = 17.6			
$\dot{q}_w, \alpha = 1.25^\circ, \phi = 0^\circ$ normalized by $\dot{q}_w, \alpha = 0^\circ$			
Re (L)	Measured	Computed	% error
.65 million	1.249	1.268	1.5
1.7 million	1.092	1.103	1.0
3.1 million	1.723	1.511	12.3

Figure 15 shows a comparison between the computed and measured heating rates along a 10-degree flare on the same projectile model. The zero-yaw and $\alpha = 1.25^\circ$ windward side are compared. The trend and overall magnitude of the data are predicted by the code. Lower heating rates measured near the cylinder-flare junction are not predicted.

Figure 16 shows a comparison between the computed and measured Stanton number along a 15-degree cone, cylinder midsection, and 10-degree flare afterbody projectile as determined in a wind tunnel test.⁷² The freestream Mach and Reynolds numbers were 4.98 and 7.9 million (based on total body length), respectively. The model was at zero yaw. The wall temperature was cooled to .17-times the freestream stagnation value of 710 R or precisely the freestream static value before the test. The heating rates on the flare afterbody are underpredicted by about 14%. This discrepancy may be due in part to the steep flare angle where rapid boundary layer thickening occurs on the flare.

VI. CONCLUSIONS

An engineering design code utilizing viscous-inviscid interaction has been developed to obtain aerodynamic and heat transfer predictions for axisymmetric projectiles at high speed. Separate solutions for inviscid and viscous flowfields are coupled by an iterative interaction model. Inviscid methods include linearized perturbation, second-order shock-expansion, and modified-Newtonian theories. The boundary layer equations are solved

⁷² Schaefer, J.W., and Ferguson, H., "Investigation of Separation and Associated Heat Transfer and Pressure Distribution on Cone-Cylinder-Flare Configurations at Mach Five," *ARS Journal*, Vol. 32, No. 5, May 1962, pp. 762-770.

using a second-order, finite-difference scheme with specified edge velocity (standard) or displacement thickness (inverse). The procedure has been formulated for supersonic and hypersonic Mach numbers, small angle-of-attack, and Reynolds numbers for laminar and turbulent flow. The capability of computing local reverse flow regions is included. Approximate methods for stagnation point, laminar, and turbulent heat transfer analysis are also included.

Computations of projectile surface pressure distribution for Mach numbers 2 thru 5 and 8 have been compared to wind tunnel measurements on several cone-cylinder-flare configurations. Computations for surface heat transfer coefficient have been compared to results obtained from wind tunnel measurements on flat plate, blunt cone, and cone-cylinder-flare models at Mach numbers 5 and 10. These tests show that the code is able to predict the surface pressure and heat transfer to a reasonable degree of accuracy. Trends in pressure and heat transfer with Mach number, Reynolds number, flare angle, and small angle-of-attack have been reproduced. Pressure distributions along the projectile surface have been integrated to yield force and moment coefficients and center of pressure predictions. These predictions reproduce wind tunnel data to a reasonable degree of accuracy. Predicted aerodynamic heat transfer distributions along the projectile surface can provide input to heat conduction codes that compute material stresses and deformations due to thermal loads.

The INTERACT code yields boundary-layer and surface profiles and heat transfer rates in about one minute of interactive run time on minicomputers. Grid generation is not required and input parameters are read from a namelist. The code includes an extensive dictionary of input parameter definitions, and issues warnings when these parameters are improperly used in an individual or global sense. The code has been written using standard FORTRAN 77 and can be run on personal computers. INTERACT is highly suitable for projectile design studies aimed at maximizing aerodynamic performance while minimizing aerodynamic heating. In addition, INTERACT can be used to test and improve various algebraic turbulence models.

INTENTIONALLY LEFT BLANK.

REFERENCES

1. Celmins, I., "Drag and Stability Tradeoffs for Flare-Stabilized Projectiles," U.S. Army Ballistic Research Laboratory, Aberdeen Proving Ground, MD., report in preparation.
2. Celmins, I., "Aerodynamic Characteristics of Fin- and Flare-Stabilized 25mm XM910 Prototypes," BRL-TR-2882, U.S. Army Ballistic Research Laboratory, Aberdeen Proving Ground, MD., Dec. 1987.
3. Mermagen, W.H., and Yalamanchili, R.J., "The Effect of Perforations on the Ballistics of a Flare-Stabilized Projectile," AIAA-86-2024, Proceedings of the 13th AIAA Atmospheric Flight Mechanics Conference, Williamsburg VA, August 18-20, 1986.
4. Garner, J.M., Zielinski, A.E., and Jamison, K.A., "Design and Testing of a Mass-Stabilized Projectile for a Small Caliber Electromagnetic Gun," BRL-MR-3744, U.S. Army Ballistic Research Laboratory, Aberdeen Proving Ground, MD, April 1989.
5. Pengelley, R., and Sweetman, B., "FMC's CAP (Combustion Augmented Plasma) Gun," International Defense Review, July 1989, pp. 813-815.
6. Hertzberg, A., Bruckner, A.P., and Bogdanoff, D.W., "Ram Accelerator: A New Chemical Method for Accelerating Projectiles to Ultrahigh Velocities," AIAA Journal, Vol. 26, No. 2, February 1988, pp. 195-203.
7. Nusca, M.J., "Computational Aerodynamics for Axisymmetric Cone-Cylinder-Flare Projectiles in Supersonic Flight," AIAA-85-1837, Proceedings of the 12th AIAA Atmospheric Flight Mechanics Conference, Snowmass CO, August 19-21, 1985.
8. McCoy, R.L., "McDRAG - A Computer Program for Estimating the Drag Coefficients of Projectiles," BRL-TR-2293, U.S. Army Ballistic Research Laboratory, Aberdeen Proving Ground, MD, Feb. 1981.
9. Donovan, W.F., and Wood, S.A., "Automatic Plotting Routines for Estimating Aerodynamic Properties of Spin Stabilized Projectiles in Flat Fire Trajectories at $2 < M < 5$," BRL-MR-3204, U.S. Army Ballistic Research Laboratory, Aberdeen Proving Ground, MD, Oct. 1982.
10. Donovan, W.F., "Hypothetical Zero Yaw Drag Trajectory of Spinning Projectiles Between $M=5$ and $M=10$," BRL-MR-3404, U.S. Army Ballistic Research Laboratory, Aberdeen Proving Ground, MD, Nov. 1984.
11. Morris, M.A., "A Computer Program to Predict the Major Aerodynamic Coefficients of Conventional Shell and Bullet Body Shapes," RARDE Memorandum Report 9/81, June 1981.
12. Donovan, W.F., Nusca, M.J., and Wood, S.A., "Automatic Plotting Routines for Estimating Static Aerodynamic Properties of Long Rod Finned Projectiles for $2 \leq M \leq 5$," BRL-MR-3123, U.S. Army Ballistic Research Laboratory, Aberdeen Proving Ground, MD, Aug. 1981.

13. Donovan, W.F., and Grollman, B.B., "Procedure for Estimating Zero Yaw Drag Coefficient for Long Rod Projectiles at Mach Numbers from 2 to 5," BRL-MR-2819, U.S. Army Ballistic Research Laboratory, Aberdeen Proving Ground, MD, Mar. 1978.
14. Donovan, W.F., "Automatic Plotting Routines for Estimating Static Aerodynamic Properties of Flared Projectiles for $2 < M < 5$," BRL-MR-3573, U.S. Army Ballistic Research Laboratory, Aberdeen Proving Ground, MD, Mar. 1987.
15. Whyte, R.H., "SPIN-73, An Updated Version of the SPINNER Computer Program," U.S. Army Picatinny Arsenal Technical Report TR-4588, November 1973.
16. Whyte, R.H., Burnett, J.R., and Hathaway, W.H., "FIN-81 A Computer Program to Predict Fin Stabilized Projectile Aerodynamic Coefficients and Stability Parameters," General Electric Armament Systems Dept., April 1981.
17. Fischer, M.A., "PRODAS User Manual - Version 3.1," General Electric Armament Systems Dept., February 1989.
18. McCoy, R.L., "Estimation of the Static Aerodynamic Characteristics of Ordnance Projectiles at Supersonic Speeds," BRL Report No. 1682, U.S. Army Ballistic Research Laboratory, Aberdeen Proving Ground, MD, Nov. 1973.
19. Vukelich, S.R., and Jenkins, J.E., "Missile Datcom: Aerodynamic Prediction of Conventional Missiles Using Component Build-Up Techniques," AIAA-84-0388, 1984.
20. Devan, L., and Mason, L.A., "Aerodynamics of Tactical Weapons to Mach Number 8 and Angle of Attack 180° : Part II, Computer Program and Users Guide," NSWC TR 81-358, Naval Surface Warfare Center, Sept. 1981.
21. Vukelich, S.R., and Jenkins, J.E., "Evaluation of Component Buildup Methods for Missile Aerodynamic Prediction," AIAA Journal of Spacecraft and Rockets, Vol. 19, No. 6, Nov/Dec 1982, pp. 481-488.
22. Sun, J., and Cummings, R.M., "Evaluation of Missile Aerodynamic Characteristics Using Rapid Prediction Techniques," AIAA Journal of Spacecraft and Rockets, Vol. 21, No. 6, Nov/Dec 1984, pp. 513-520.
23. Mikhail, A.G., "Interactive Input for Projectile Fast Design Codes Package," BRL-MR-3631, U.S. Army Ballistic Research Laboratory, Aberdeen Proving Ground, MD, October 1987.
24. Sturek, W.B., Dwyer, H.A., Kayser, L.D., Nietubicz, C.J., Reklis, R.P., and Opalka, K.O., "Computations of Magnus Effects for a Yawed, Spinning Body of Revolution," AIAA Journal, Vol. 16, No. 7, July 1978, pp. 687-692.
25. Sturek, W.B., Mylin, D.C., and Bush, C.C., "Computational Parametric Study of the Aerodynamics of Spinning Slender Bodies at Supersonic Speeds," AIAA-80-1585, Proceedings of the 7th AIAA Atmospheric Flight Mechanics Conference, August 11-13, 1980.
26. Nietubicz, C.J., Danberg, J.E., and Inger, G.R., "A Theoretical and Experimental Investigation of a Transonic Projectile Flow Field," BRL-MR-3291, U.S. Army Ballistic Research Laboratory, Aberdeen Proving Ground, MD., July 1983.

27. Pletcher, R.H., "Prediction of Incompressible Turbulent Separating Flow," Journal of Fluids Engineering, Vol. 100, Dec. 1978, pp. 427-433.
28. Kwon, O., and Pletcher, R.H., "Prediction of Incompressible Separated Boundary Layers Including Viscous-Inviscid Interaction," Transactions of the ASME, Vol. 101, Dec. 1979, pp. 466-472.
29. Williams, B.R., "The Prediction of Separated Flow Using A Viscous-Inviscid Interaction Method," Aeronautical Journal, May 1985, pp. 185-197.
30. Im, B.J., "A Coupled Viscid-Inviscid Calculation Method for the Prediction of Unsteady Separated Flows Over An Airfoil," AIAA-88-0566, Proceedings of the 26th AIAA Aerospace Sciences Meeting, Reno NV, Jan. 11-14, 1988.
31. Sedney, R., "Aerodynamic Heating Problems In Shell Design," BRL Report No. 1043, U.S. Army Ballistic Research Laboratory, Aberdeen Proving Ground, MD, March 1958.
32. Van Driest, E.R., "The Problem of Aerodynamic Heating," Aeronautical Engineering Review, Vol. 15, No. 10, October 1956, pp. 26-41.
33. Rubesin, M.W., and Johnson, H.A., "A Critical Review of Skin-Friction and Heat-Transfer Solutions of the Laminar Boundary Layer of a Flat Plate," Transactions of the ASME, Vol. 71, No. 4, May 1949, pp. 358-388.
34. Young, G.B., and Janssen, E., "The Compressible Boundary Layer," Journal of Aeronautical Sciences, Vol. 19, April 1952, pp. 229-236.
35. Eckert, E.R., "Engineering Relations for Friction and Heat Transfer to Surfaces in High Velocity Flow," Journal of Aeronautical Sciences, Vol. 22, No. 8, August 1955, pp. 585-587.
36. Fay, J.A., and Kemp, N.H., "Theory of Stagnation-Point Heat Transfer in a Partially Ionized Diatomic Gas," AIAA Journal, Vol. 1, No. 12, Dec. 1963, pp. 2741-2751.
37. Crabtree, L.F., Dommett, R.L., and Woodley, J.G., "Estimation of Heat Transfer to Flat Plates, Cones and Blunt Bodies," RAE TR No. 3637, July 1965.
38. Fancett, R.K., "Heat Transfer to Slender Projectiles at Mach Numbers Between 5 and 10," RARDE Memorandum Report 2/70, 1970.
39. DeJarnette, F.R., Hamilton, H.H., Weilmuenster, K.J., and Cheatwood, F.M., "A Review of Some Approximate Methods Used in Aerodynamic Heating Analyses," AIAA Journal of Thermophysics, Vol. 1, No. 1, Jan. 1987, pp. 5-12.
40. Hoffman, K.A., Wilson, D.E., and Hamburger, C., "Aerothermodynamic Analyses of Projectiles at Hypersonic Speeds," AIAA-2185, Proceedings of the 7th AIAA Applied Aerodynamics Conference, Seattle WA, July 31 to August 2, 1989.
41. Anderson, J.D., Modern Compressible Flow with Historical Perspective, McGraw-Hill, 1982.
42. Liepmann, H.W., and Rosko, R.A., Elements of Gasdynamics, Wiley, NY, 1957 (pp. 227-230).

43. Eggers, A.J., Savin, R.C., and Syvertson, C.A., "The Generalized Shock- Expansion Method and Its Application to Bodies Traveling at High Supersonic Airspeeds," Journal of Aeronautical Sciences, Vol. 22, No. 4, April 1955, pp. 231-238.
44. Syvertson, C.A., and Dennis, D.H., "A Second-Order Shock-Expansion Method Applicable to Bodies of Revolution Near Zero Lift," NACA TN-3527, Jan. 1956.
45. Ames Research Staff, "Equations, Tables, and Charts for Compressible Flow," NACA Report-1135, NASA Ames Aeronautical Laboratory, Moffet Field CA, 1958.
46. Robinson, M.L., "Boundary Layer Effects in Supersonic Flow Over Cylinder- Flare Bodies," WRE-Report-1238, Australian Defense Scientific Service, Weapons Research Establishment, July 1974.
47. Taylor, G.I., and MacColl, J.W., "The Air Pressure on a Cone Moving at High Speed," Proc. Royal Soc. (London), Ser. A, Vol. 139, pp. 278-311.
48. Anderson, J.D., Hypersonic and High Temperature Gas Dynamics, McGraw-Hill, 1989.
49. Cebeci, T., and Smith, A.M.O., Analysis of Turbulent Boundary Layers, Academic Press, 1974.
50. Bradshaw, P., Cebeci, T., and Whitelaw, J.H., Engineering Calculation Methods for Turbulent Flow, Academic Press, 1981.
51. Brown, S.N., and Stewartson, K., "Laminar Separation," Annual Review of Fluid Mechanics, Vol. 1, 1969.
52. Stewartson, K., and Williams, P.G., Mathematika, Vol. 20, 1973, pp. 98-108.
53. Flugge-Lotz, I., and Reyhner, T.A., "The Interaction of a Shock Wave with a Laminar Boundary Layer" International Journal of Non-Linear Mechanics, Vol. 3, 1968, pp. 173-199.
54. Williams, P.G., " A Reverse Flow Computation In The Theory of Self-Induced Separation," Lecture Notes in Physics, Vol. 35, Proceedings of the 4th International Conference on Numerical Methods in Fluid Dynamics, Springer-Verlag, 1975.
55. Cebeci, T., "Separated Flows and Their Representation by Boundary Layer Equations," Report ONR-CR 215-234-2, Office of Naval Research, Arlington, VA, 1976.
56. Carter, J.E., "A New Boundary-Layer Interaction Technique for Separated Flows," NASA TM-78690, June 1978.
57. Kaufmann, K.C., and Hoffman, G.H., "A Unified Approach to Direct and Inverse Boundary Layer Solutions," International Journal for Numerical Methods in Fluids, Vol. 8, 1988, pp. 1367-1388.
58. McDonald, H., and Briley, W.R., "A Survey of Recent Work on Interacting Boundary- Layer Theory for Flow With Separation," Numerical and Physical Aspects of Aerodynamic Flows II, (Cebeci, ed.) Springer-Verlag, 1984.
59. Briley, W.R., and McDonald, H., "Numerical Prediction of Incompressible Separation Bubbles," Journal of Fluid Dynamics, Vol. 69, Pt. 4, 1975, pp. 631-656.

60. Keller, H.B., "A New Difference Scheme for Parabolic Problems," Numerical Solutions of Partial Differential Equations II, (Bramble ed.) Academic Press, 1970.
61. Cebeci, T., "An Inverse Boundary-Layer Method for Compressible Laminar and Turbulent Boundary Layers," AIAA Journal of Aircraft, Vol. 13, No. 9, Sept. 1976, pp. 709-717.
62. Anderson, D.A., Tannehill, J.C., and Pletcher, R.H., Computational Fluid Dynamics and Heat Transfer, Hemisphere Publishing Corp., McGraw-Hill, 1984.
63. Cebeci, T., Khalil, E.E., and Whitelaw, J.H., "Calculation of Separated Boundary-Layer Flows," AIAA Journal, Vol. 17, No. 12, Dec. 1979, pp. 1291-1292.
64. Carter, J.E., "Inverse Solutions For Laminar Boundary-Layer Flows With Separation and Reattachment," NASA TR R-447, Nov. 1975.
65. Edwards, D.E., Carter, J.E., and Smith, F.T., "Analysis of Three-Dimensional Separated Flow with the Boundary-Layer Equations," AIAA Journal, Vol. 25, No. 3, March 1987, pp. 380-387.
66. Jackson, C.M., Sawyer, W.C., and Smith, R.S., "A Method For Determining Surface Pressures on Blunt Bodies of Revolution at Small Angles of Attack in Supersonic Flow," NASA TN D-4865, November 1968.
67. Washington, W.D., and Humphrey, J.A., "Pressure Measurements on Four Cone-Cylinder-Flare Configurations at Supersonic Speeds," U.S. Army Missile Command Report No. RD-TM-69-11, 20 Oct. 1969.
68. Gray, J.D., "Laminar Boundary-Layer Separation on Flared Bodies at Supersonic and Hypersonic Speeds," U.S. Air Force Systems Command AEDC-TR-64-277, Jan. 1965.
69. Dennis, D.H., "The Effects of Boundary-Layer Separation Over Bodies of Revolution With Conical Tail Flares," NACA RM-A57130, Dec. 1957.
70. Holden, M.S., "An Experimental Investigation of Turbulent Boundary Layers at High Mach Number and Reynolds Number," Cornell Aeronautical Laboratory (Calspan), Buffalo NY, Report No. AB-5072-A-1, Nov. 1972 (see also NASA CR-112147).
71. Goodrich, W.D., Li, C.P., Houston, C.K., Chiu, P.B., and Olmedo, L., "Numerical Computations of Orbiter Flowfields and Laminar Heating Rates," AIAA Journal of Spacecraft and Rockets, Vol. 14, No. 5, May 1977, pp. 257-264.
72. Schaefer, J.W., and Ferguson, H., "Investigation of Separation and Associated Heat Transfer and Pressure Distribution on Cone-Cylinder-Flare Configurations at Mach Five," ARS Journal, Vol. 32, No. 5, May 1962, pp. 762-770.

INTENTIONALLY LEFT BLANK.

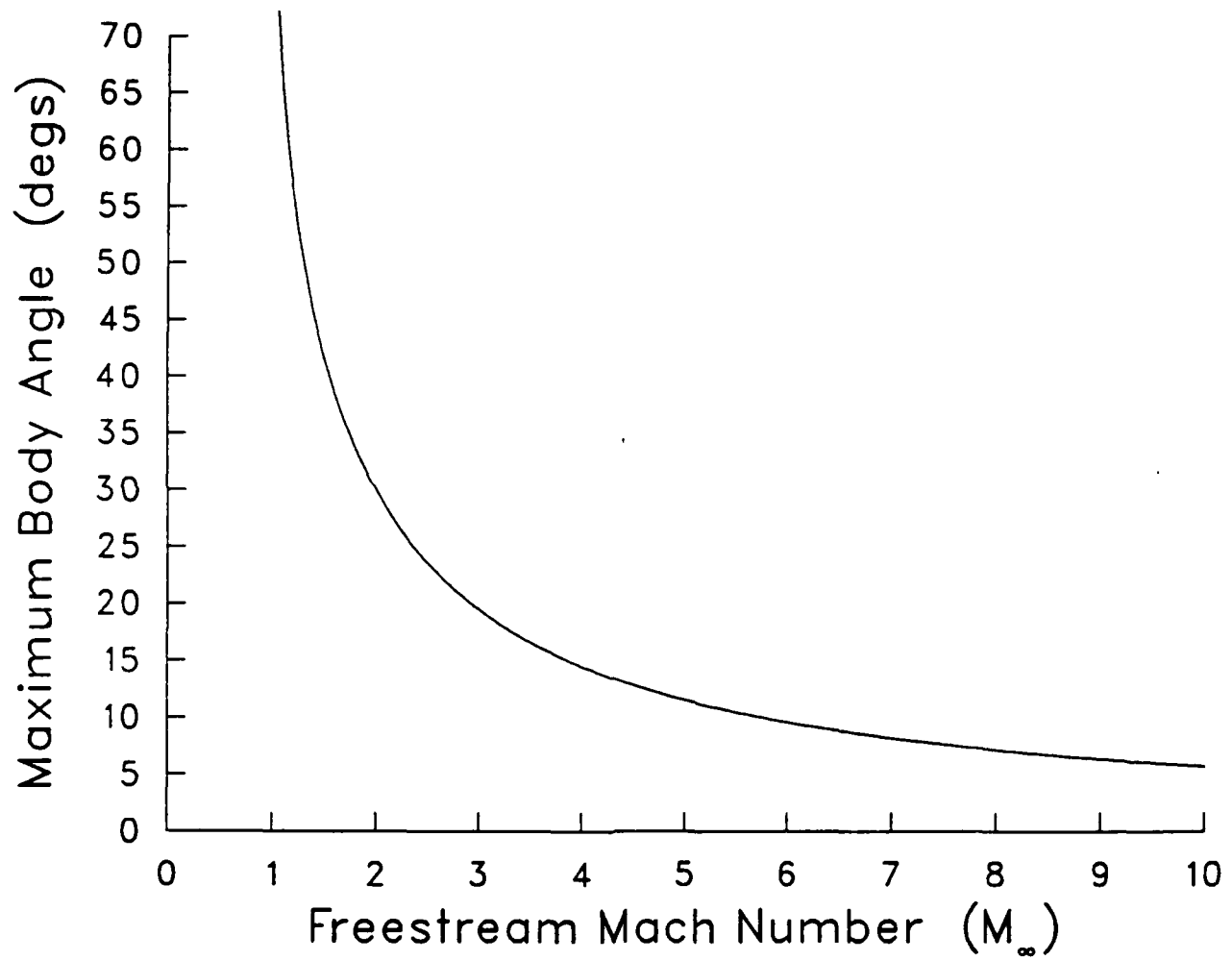


Figure 1. Linearized Perturbation Theory – Maximum Body Angle vs. Mach Number

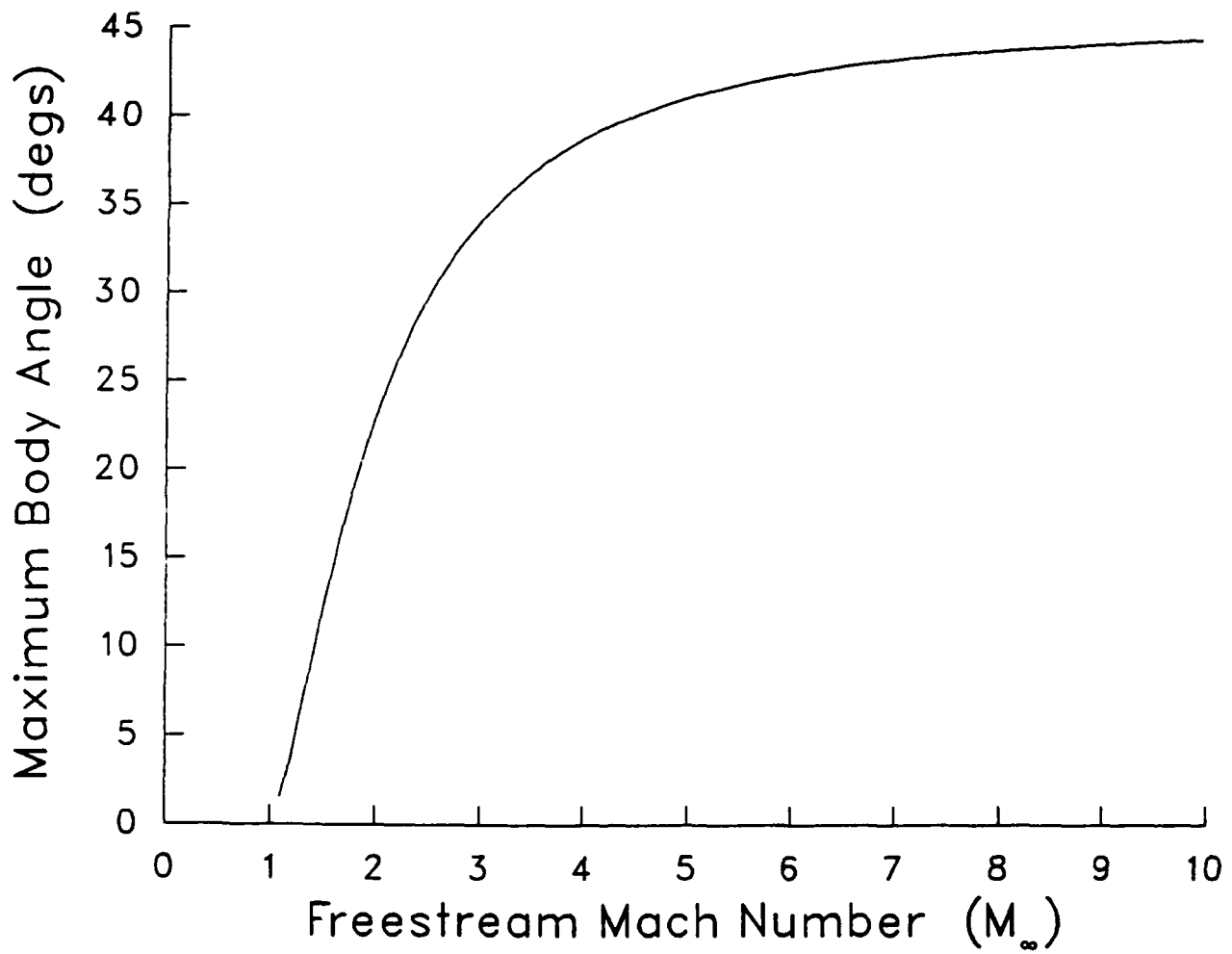


Figure 2. Oblique Shock Theory – Maximum Body Angle vs. Mach Number

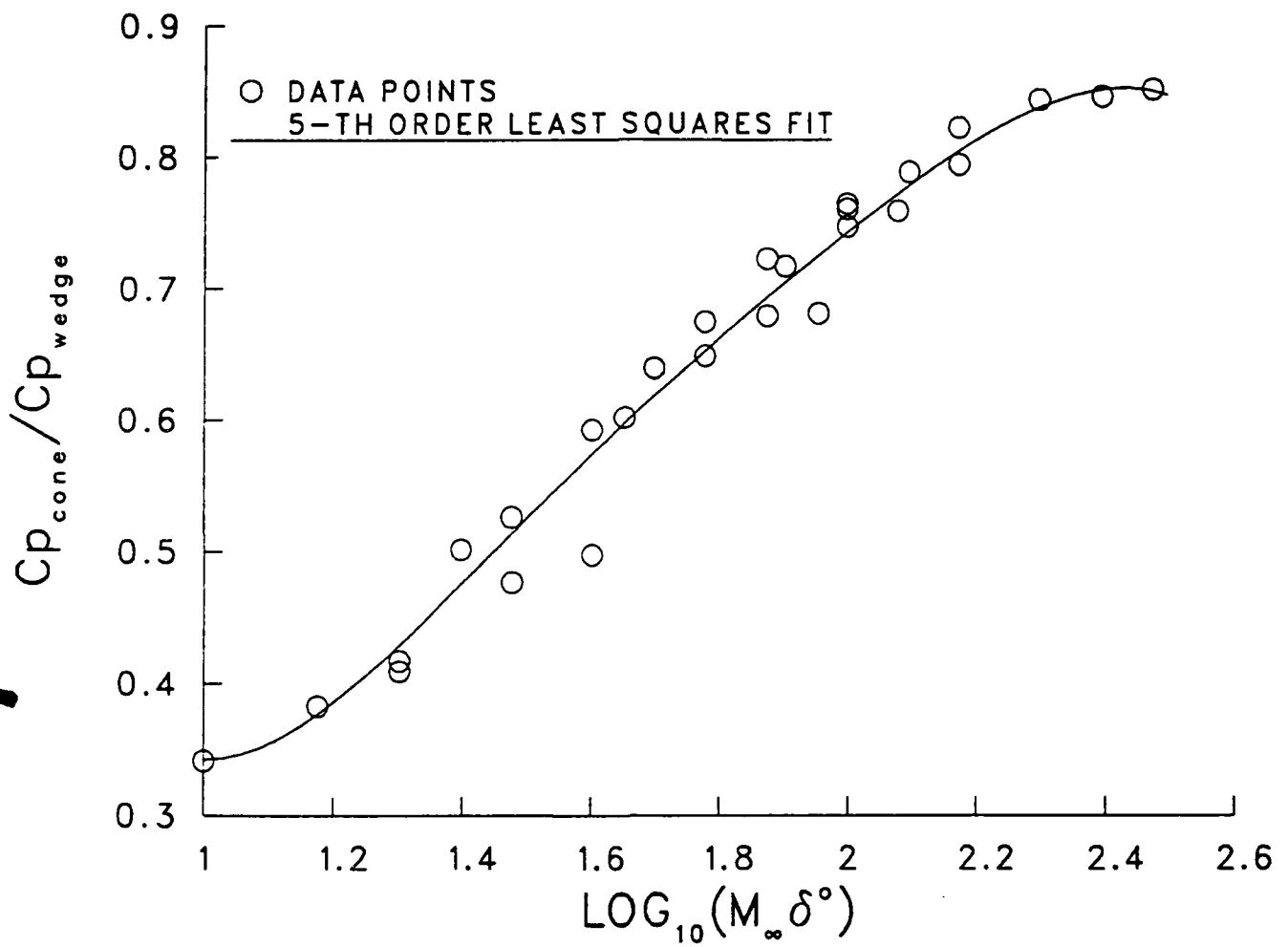


Figure 3. Variation of $(C_p)_{cone}/(C_p)_{wedge}$ with $\text{LOG}_{10}(M_\infty \delta^\circ)$.

5° Cone - Cylinder - 4° Flare
 $\alpha = 0^\circ$, $Re(D) = 494000$, $Re(L) = 7600000$

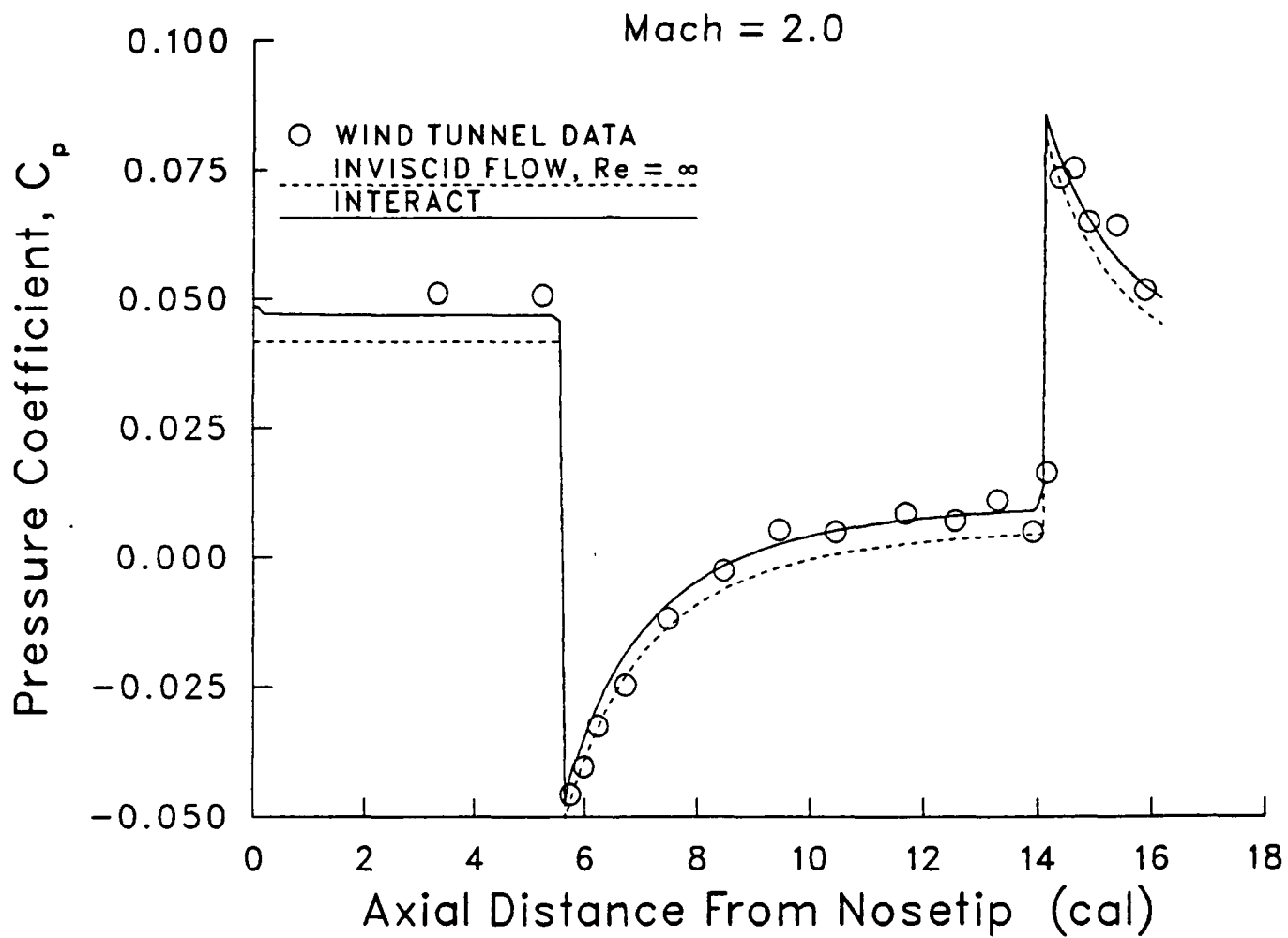


Figure 4. Wind Tunnel Data (C_p) vs. Inviscid Flow ($Re = \infty$) and INTERACT; 4° Flare, Mach = 2

5° Cone - Cylinder - 4° Flare
 $\alpha = 0^\circ$, $Re(D) = 494000$, $Re(L) = 7600000$

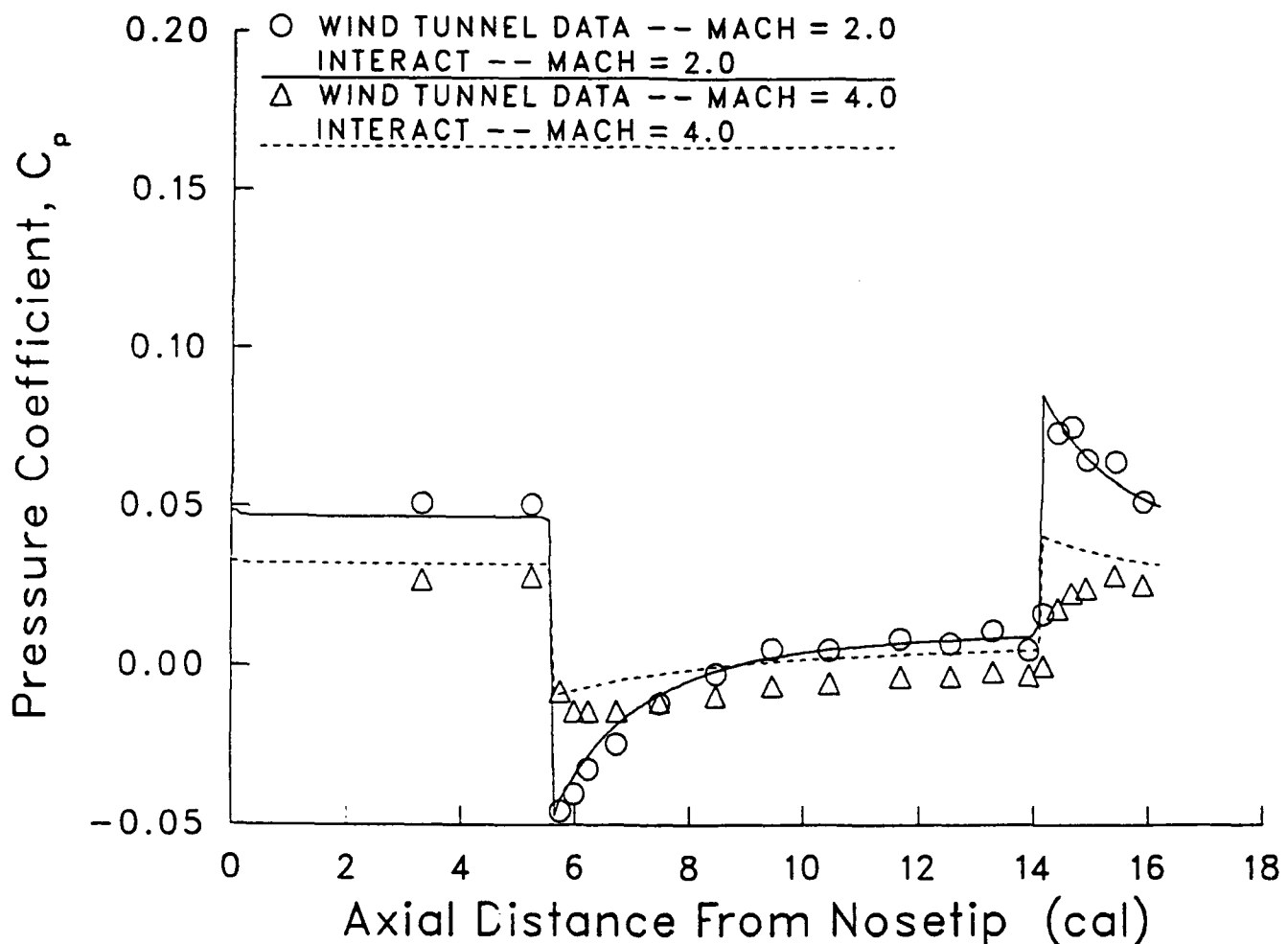


Figure 5. Comparison of Wind Tunnel Data (C_p) with INTERACT Results; 4° Flare, Mach = 2,4

5° Cone - Cylinder - 6° Flare
 $\alpha = 0^\circ$, $Re(D) = 494000$, $Re(L) = 7600000$

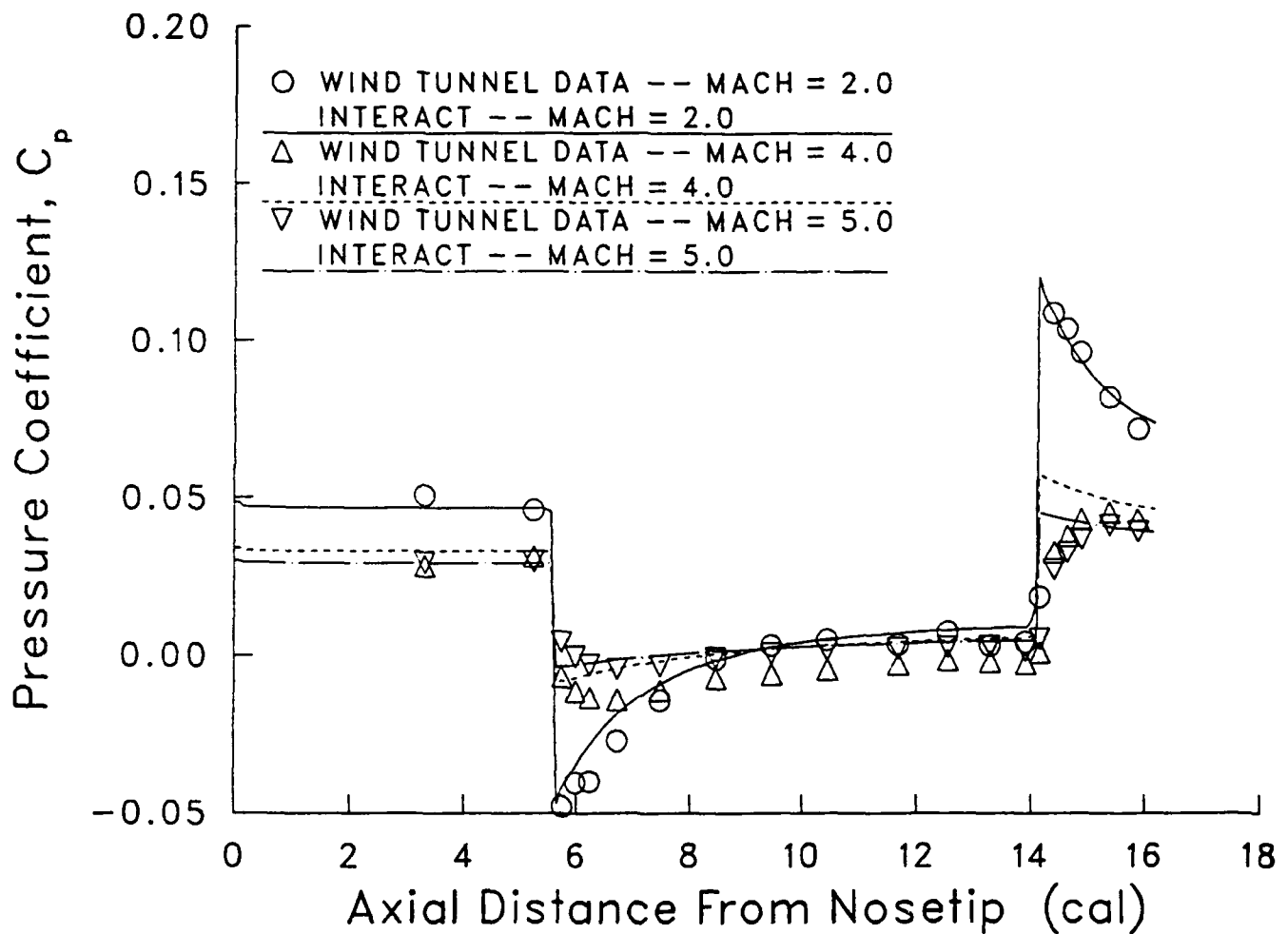


Figure 6. Comparison of Wind Tunnel Data (C_p) with INTERACT Results; 6° Flare, Mach = 2,4,5

5° Cone – Cylinder – 8° Flare
 $\alpha = 0^\circ$, $Re(D) = 494000$, $Re(L) = 7600000$

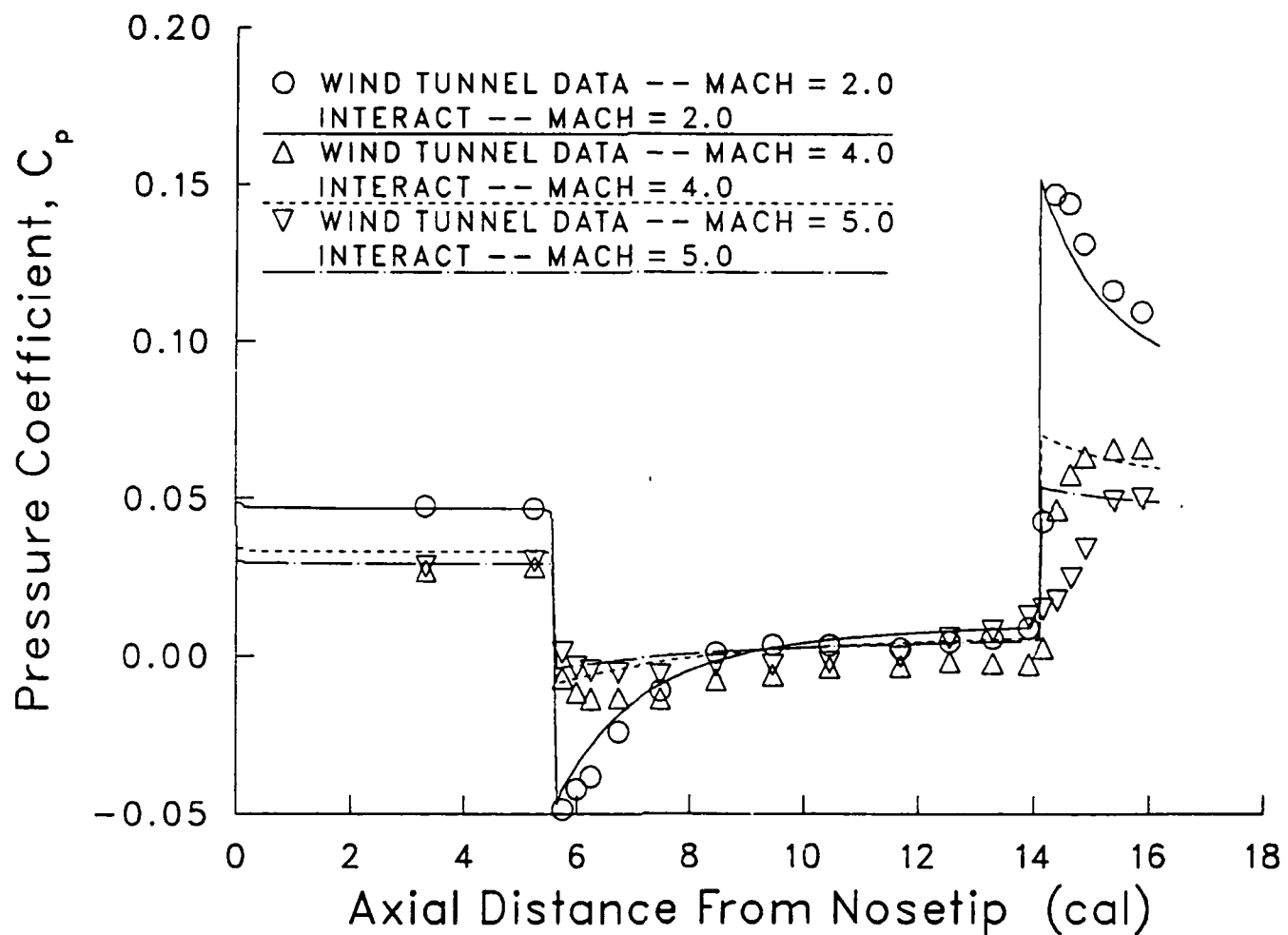


Figure 7. Comparison of Wind Tunnel Data (C_p) with INTERACT Results; 8° Flare, Mach = 2,4,5

10° Cone - Cylinder - 20° Flare
 $\alpha = 0^\circ$, $Re(D) = 2.3$ mill, $Re(L) = 18$ mill

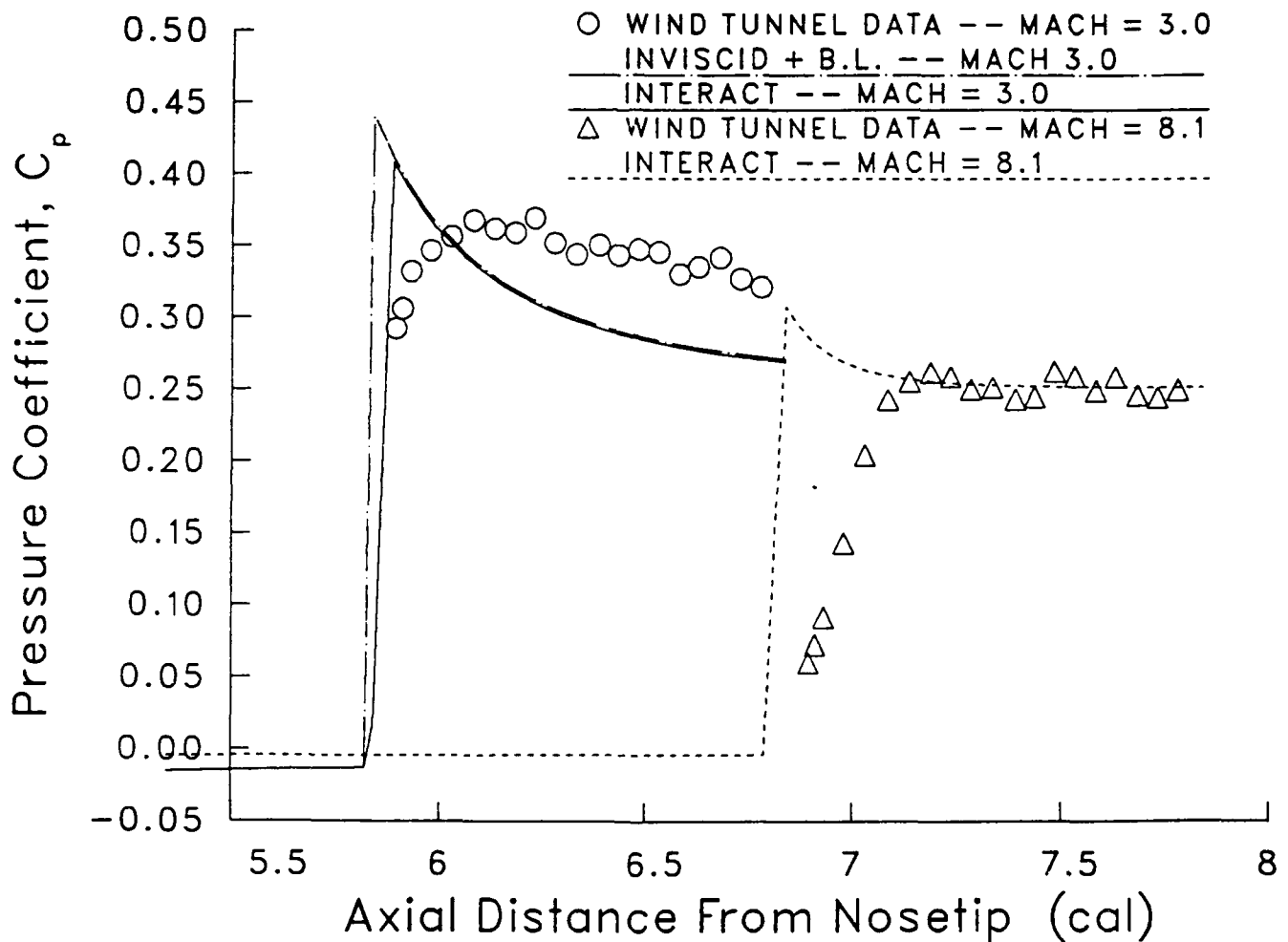


Figure 8. Comparison of Wind Tunnel Data (C_p) with INTERACT Results; 20° Flare, Mach = 3,8.1

5° Cone - Cylinder - 6° Flare
 $\alpha = 1^\circ$, $Re(D) = 494000$, $Re(L) = 7600000$

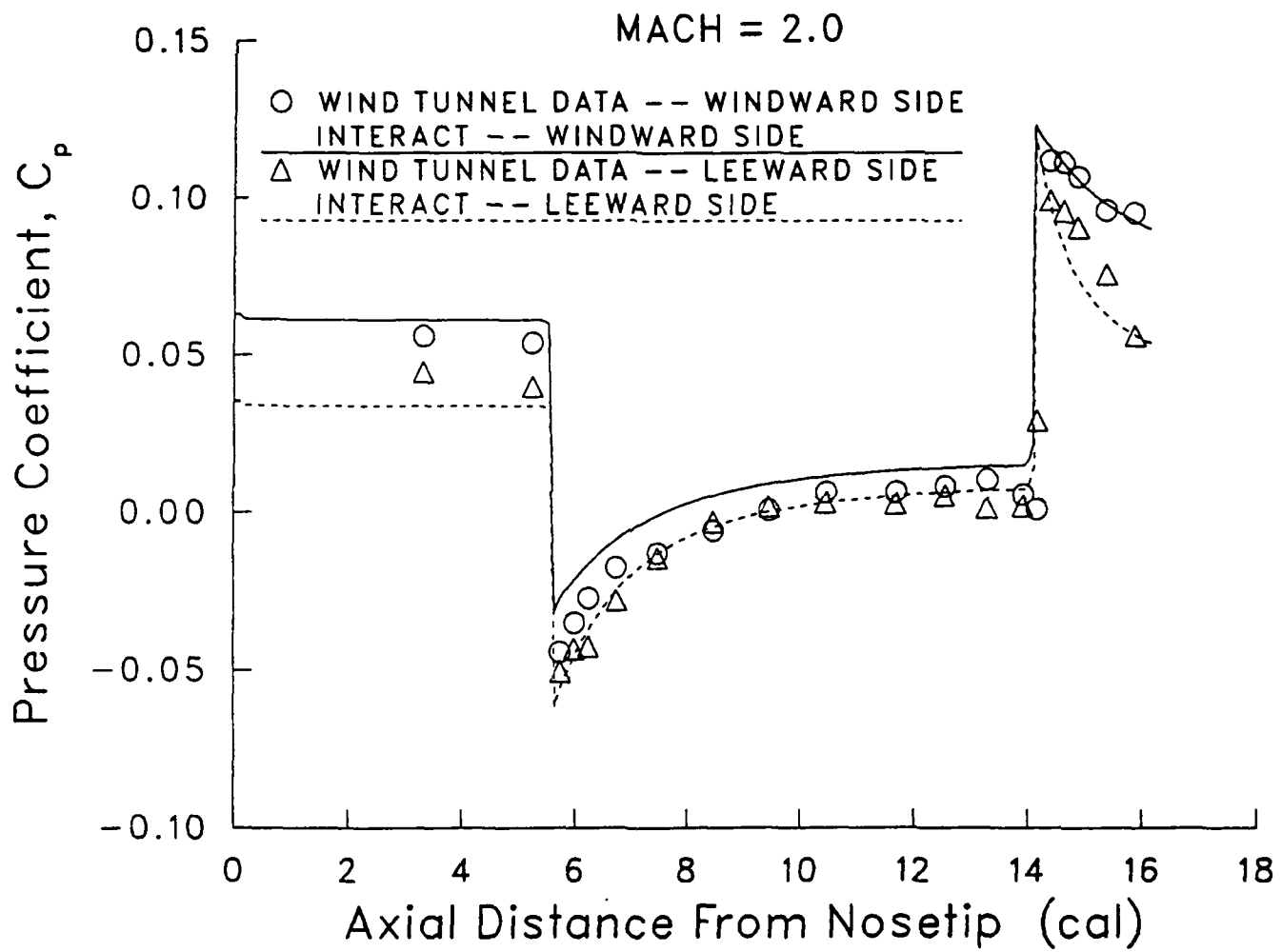


Figure 9. Comparison of Wind Tunnel Data (C_p) with INTERACT Results; 6° Flare, Mach = 2, $\alpha = 1^\circ$

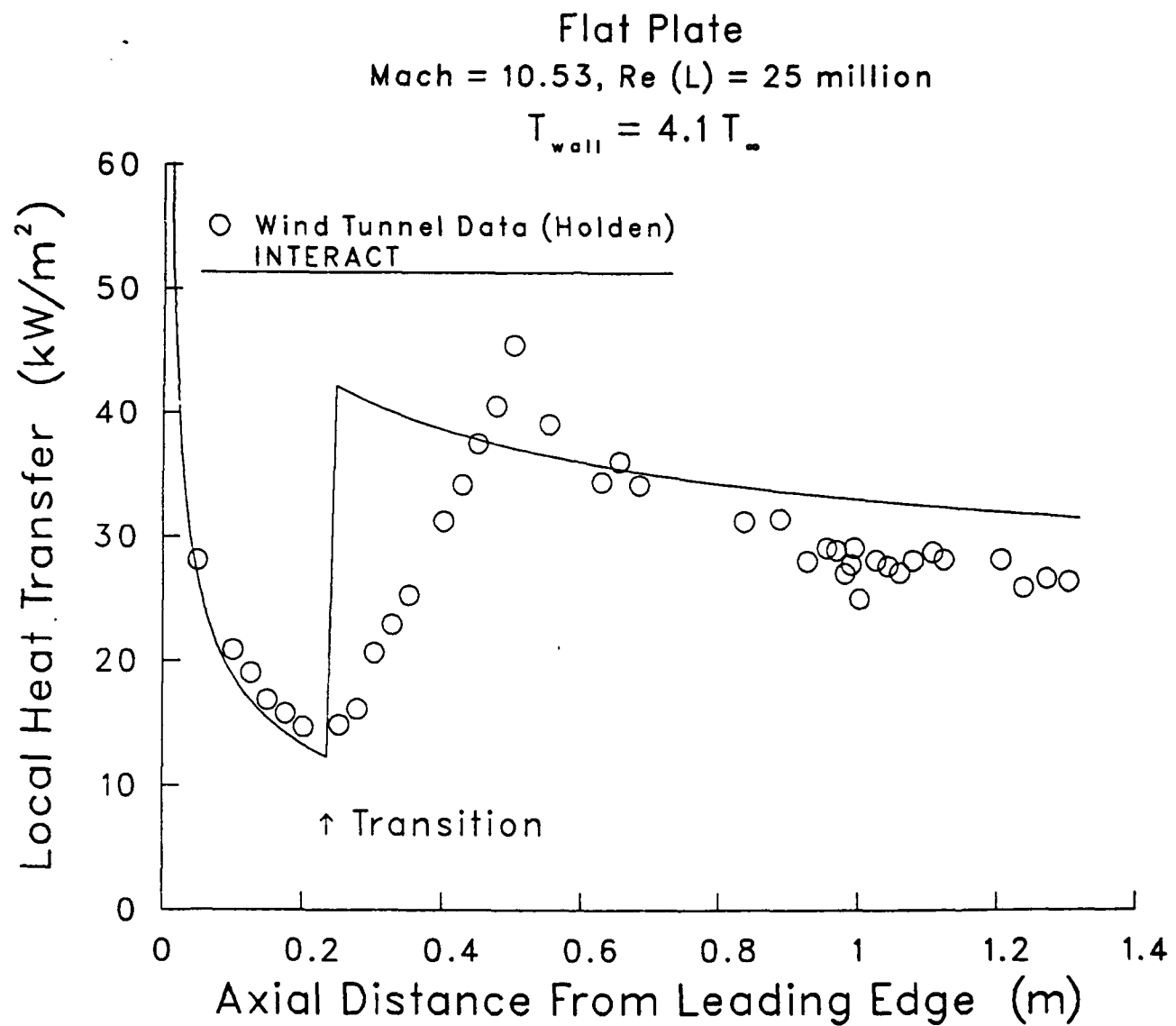


Figure 10. Comparison of Wind Tunnel Data (\dot{q}_w) with INTERACT Results; Flat Plate, Mach = 10.53

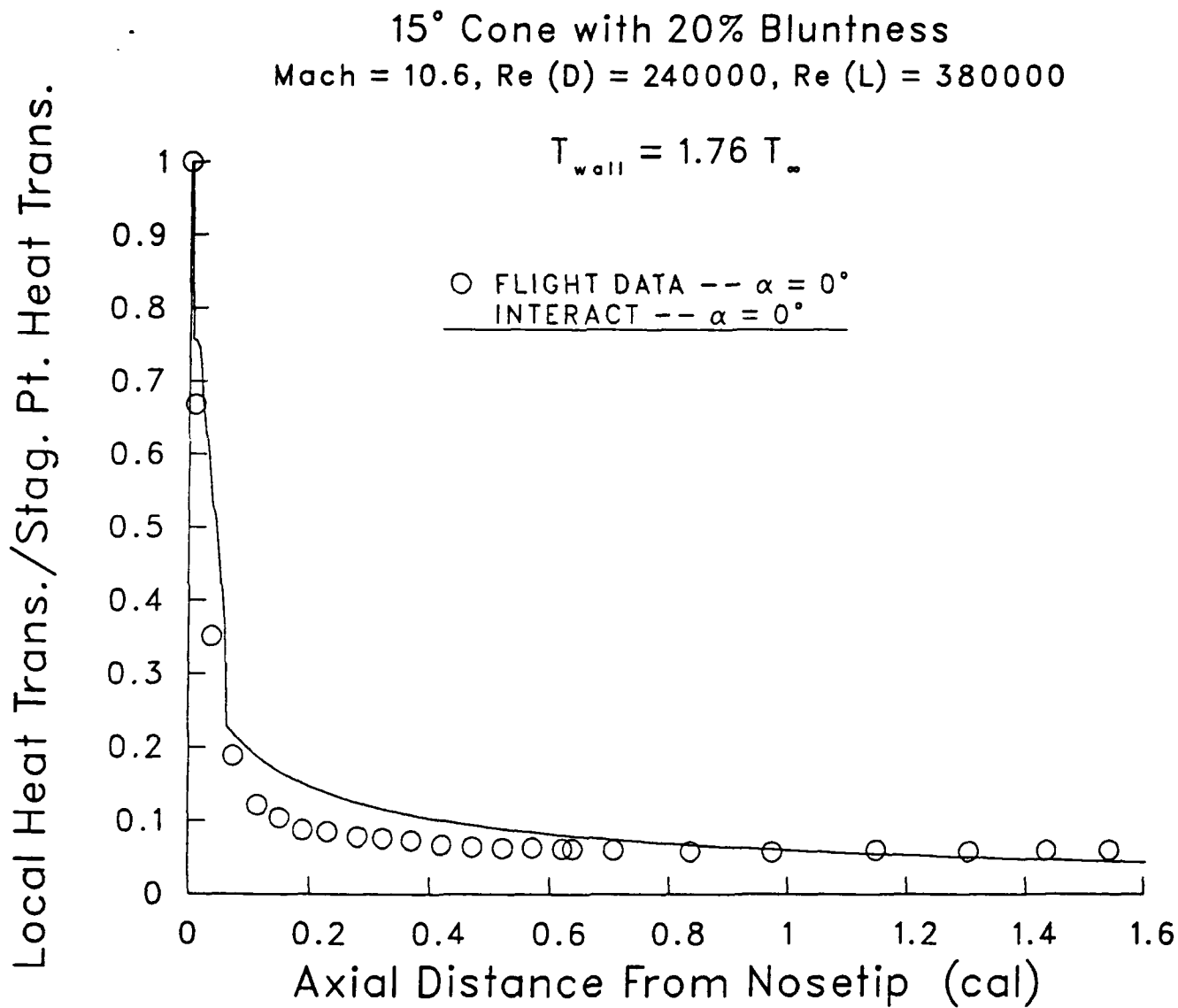


Figure 11. Comparison of Wind Tunnel Data (q_w) with INTERACT Results; Blunt Cone, Mach = 10.6

RARDE 5° Flare
Mach = 5.2, Re (D) = 84000, Re (L) = 1710000

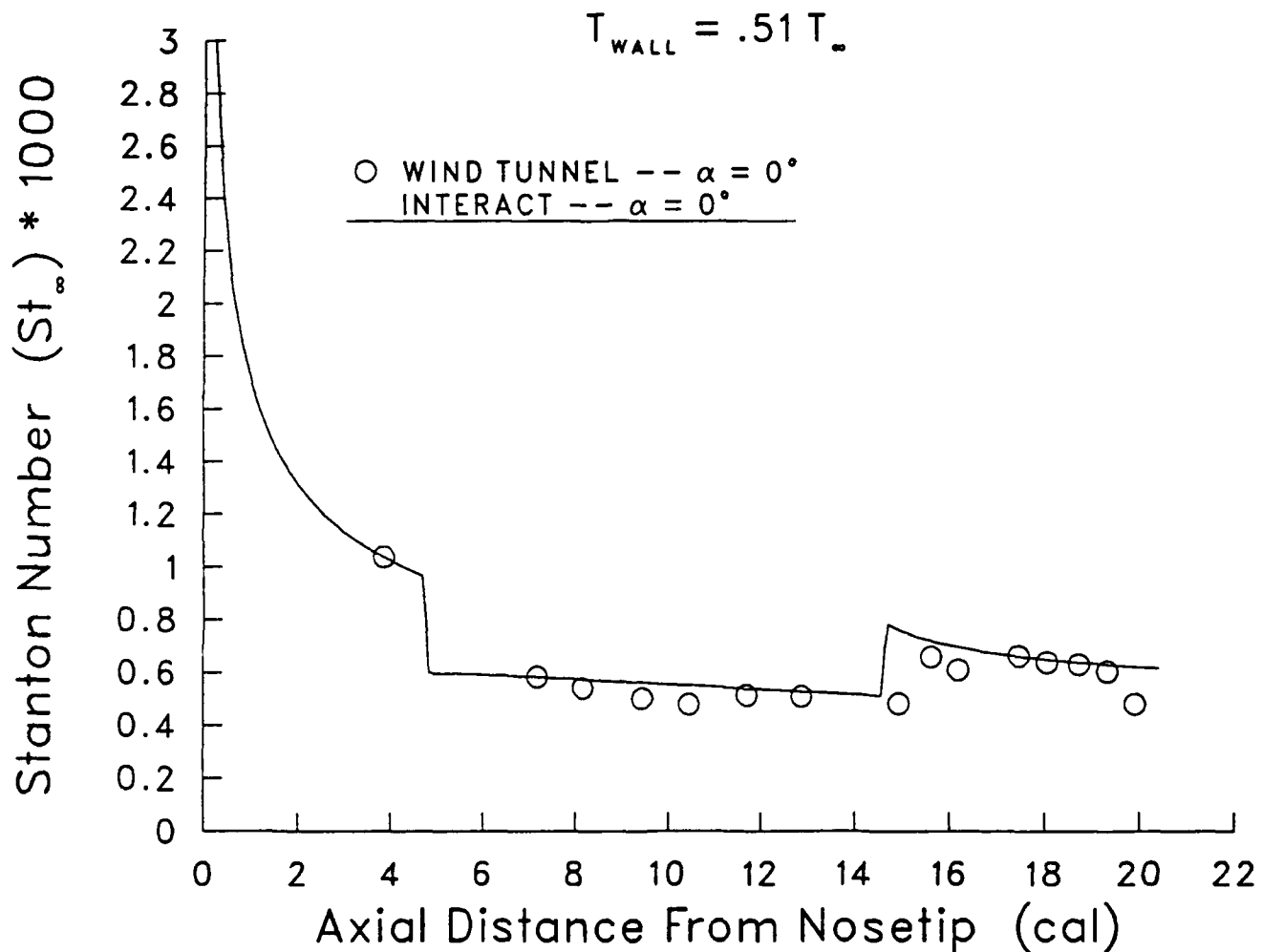


Figure 12. Comparison of Wind Tunnel Data (q_w) with INTERACT Results; 5° Flare, Mach = 5.2

RARDE 5° Flare

Mach = 5.2, Re (D) = 84000, Re (L) = 1710000

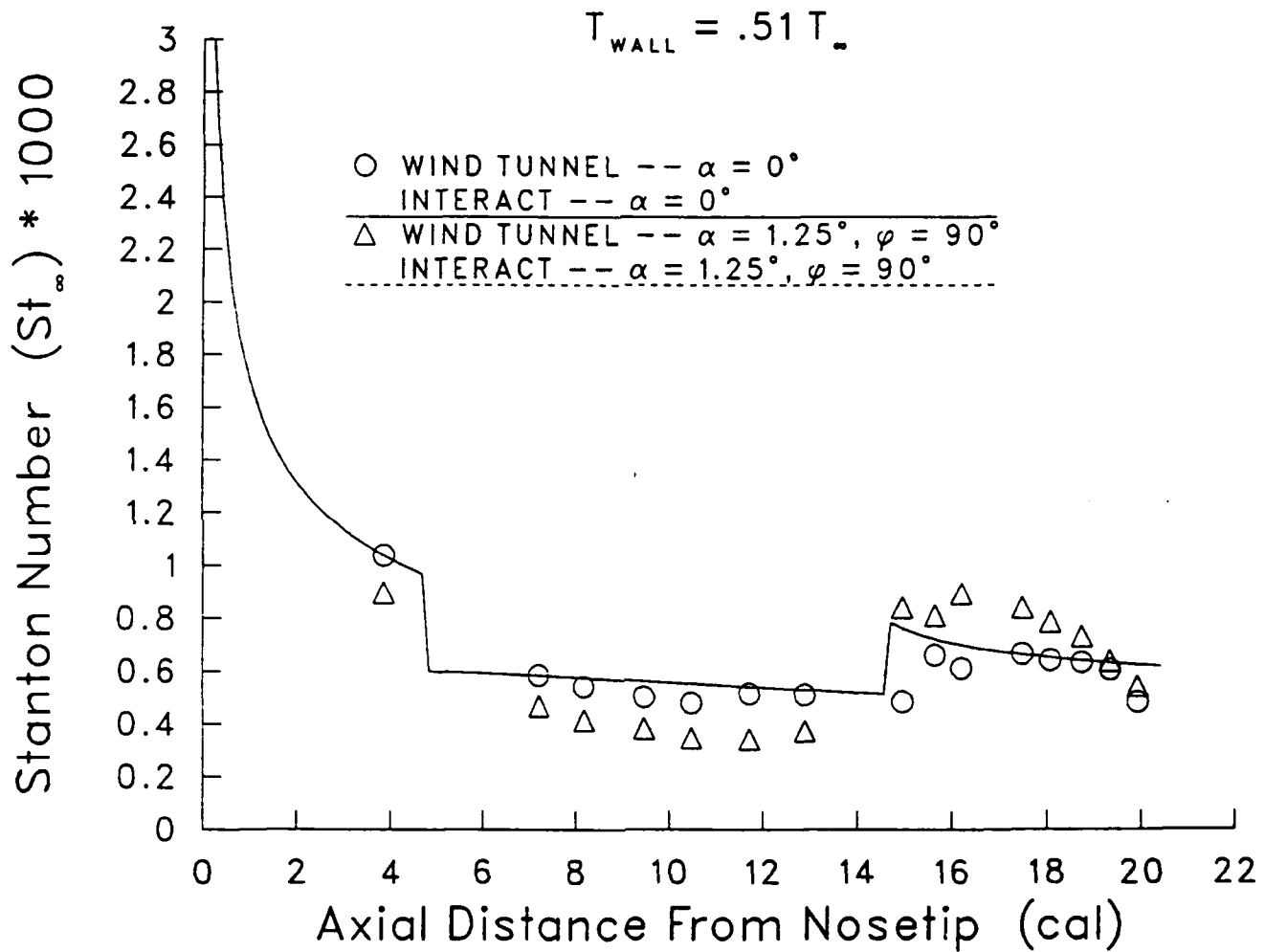


Figure 13. Comparison of Wind Tunnel Data (q_w) with INTERACT Results; 5° Flare, Mach = 5.2, $\alpha = 0^\circ$ and 1.25°

RARDE 5° Flare

Mach = 5.2, Re (D) = 84000, Re (L) = 1710000

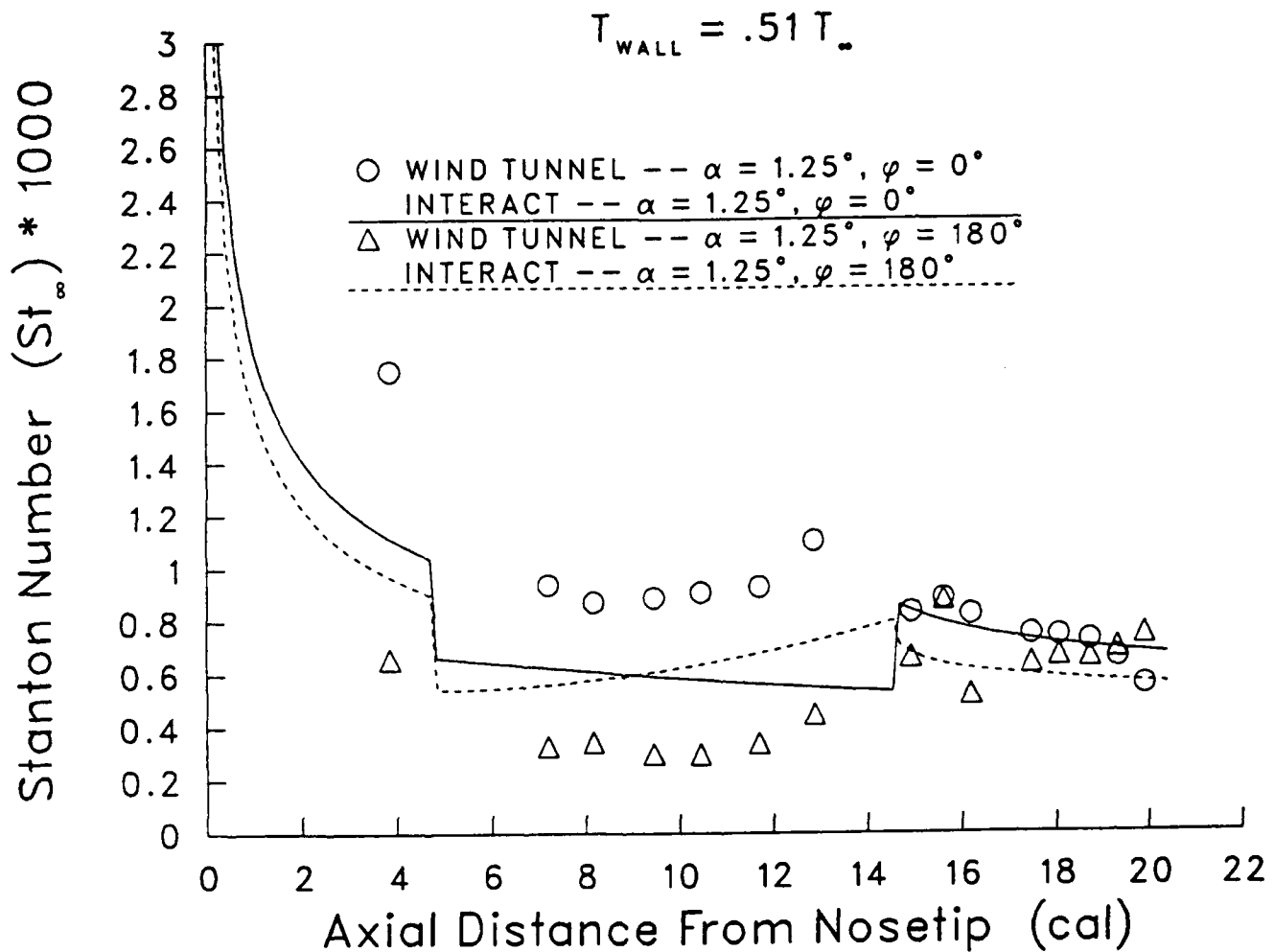


Figure 14. Comparison of Wind Tunnel Data (q_w) with INTERACT Results; 5° Flare, Mach = 5.2, $\alpha = 1.25^\circ$

RARDE 10° Flare
Mach = 5.2, Re (D) = 84000, Re (L) = 1710000

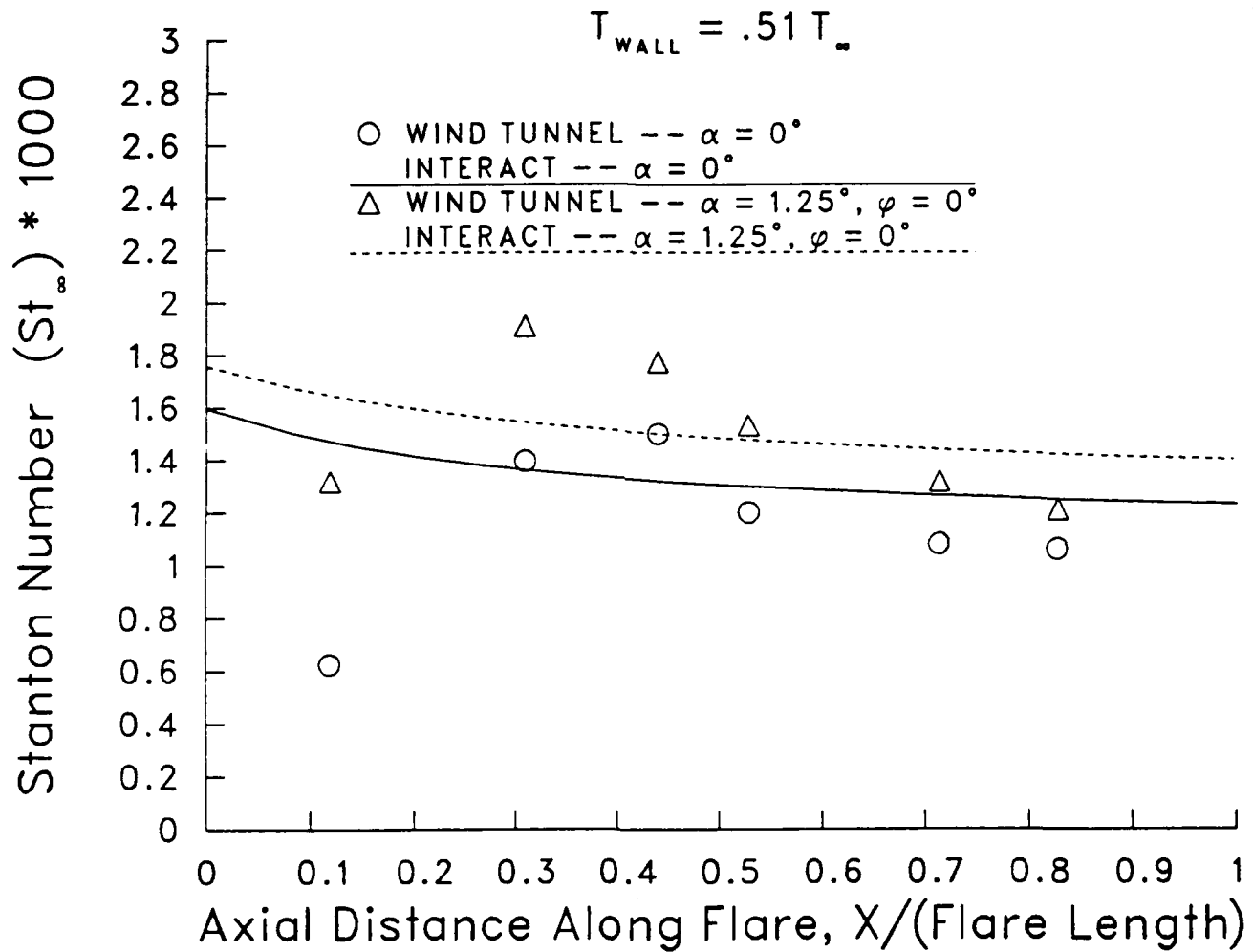


Figure 15. Comparison of Wind Tunnel Data (q_w) with INTERACT Results; 10° Flare, Mach = 5.2, $\alpha = 0^\circ$ and 1.25°

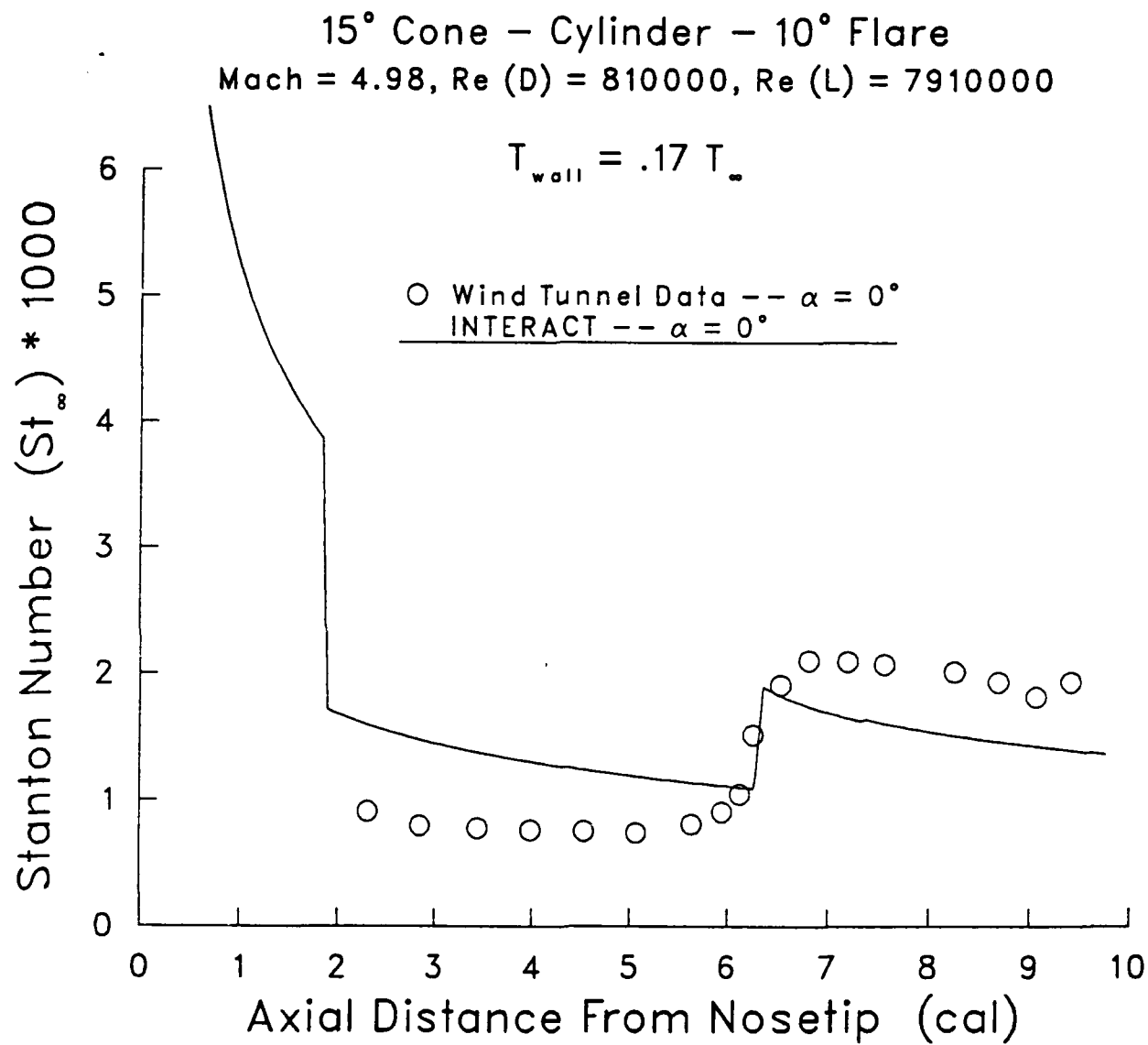


Figure 16. Comparison of Wind Tunnel Data (\dot{q}_w) with INTERACT Results; 10° Flare, Mach = 4.98

List of Symbols

a	speed of sound
A	source strength, $f'(\xi)$
C_D	pressure drag coefficient, Equation 67
C_f	skin friction coefficient, $2\tau_w/(\rho V_\infty^2)$
C_h	heat transfer coefficient, $\dot{q}_w/(T_r - T_w)$
C_N	normal force coefficient, Equation 68
C_M	pitching moment coefficient, Equation 69
C_p	pressure coefficient, $2(p - p_\infty)/(\rho_\infty V_\infty^2) = 2(p - p_\infty)/(\gamma p_\infty M_\infty^2)$
c_p	specific heat at constant pressure
c_v	specific heat at constant volume
D	characteristic diameter; caliber diameter of the projectile
D/Dt	$\partial/\partial t + u\partial/\partial x + v\partial/\partial y + w\partial/\partial z$
e	internal energy
f	dimensionless stream function
H	total enthalpy
h	static enthalpy
L	characteristic length; total length of the projectile
L_m	boundary layer mixing length
M	Mach number, V/a
n	number of body surface points
p	static pressure
Pr	Prandtl number, $\mu c_p/k$
q	heat transfer per unit time per unit area
q_∞	dynamic pressure, $1/2\rho_\infty V_\infty^2$
r	radial coordinate, $(y^2 + z^2)^{1/2}$
Re	Reynolds number, $\rho V L / \mu$
\mathfrak{R}	specific gas constant
s	entropy
St	Stanton number, $\dot{q}/(\rho u c_p (T_r - T_w))$
T	temperature
t	time
u, v, w	velocity components in the cartesian coordinate system
V	magnitude of \vec{V} or $(u^2 + v^2 + w^2)^{1/2}$
\vec{V}	velocity vector, $\vec{V} = u\hat{i} + v\hat{j} + w\hat{k}$
x, y, z	spacial cartesian coordinates
$\nabla \cdot \vec{V}$	$\frac{\partial u}{\partial x} + \frac{\partial v}{\partial y} + \frac{\partial w}{\partial z}$
$\nabla \vec{V}$	$(\frac{\partial u}{\partial x})\hat{i} + (\frac{\partial v}{\partial y})\hat{j} + (\frac{\partial w}{\partial z})\hat{k}$
$\nabla \times \vec{V}$	$(\frac{\partial w}{\partial y} - \frac{\partial v}{\partial z})\hat{i} + (\frac{\partial u}{\partial z} - \frac{\partial w}{\partial x})\hat{j} + (\frac{\partial v}{\partial x} - \frac{\partial u}{\partial y})\hat{k}$
$ $	absolute value

Greek Symbols

α	angle of attack
----------	-----------------

β	$(M^2 - 1)^{1/2}$
Γ	Van Driest damping length
γ	ratio of specific heats, c_p/c_v
δ	local body surface slope
δ^*	boundary layer displacement thickness, $\int_0^y (1 - (\rho u / \rho_e u_e)) dy$
ϵ_m	boundary layer eddy viscosity
θ	shock wave angle
λ	pressure gradient parameter, $(2\xi/u_e) du_e/d\xi$
μ	molecular viscosity
$\tilde{\mu}$	Mach angle, $\arcsin(1/M)$
ν	Prandtl-Meyer expansion angle (Equ. 16)
ξ, η	transformed coordinates
ρ	density
σ	body surface distance
τ	shear stress
Φ	velocity potential scalar, $\nabla \Phi \equiv \vec{V}$
$\tilde{\Phi}$	perturbation velocity potential scalar, $\tilde{\Phi} = \Phi - V_\infty x$
ϕ	circumferential body angle, $\phi = 0^\circ$ for windward, $\phi = 180^\circ$ for leeward
ψ	stream function, $\psi_y = r^k \rho u, \psi_x = r^k \rho v$
Ω	wind-axis circumferential body angle, $\Omega = \phi - 90^\circ$
ω_{tr}	boundary layer intermittency factor

Superscripts

i	iteration level
k	1 for axisymmetric, 0 for two-dimensional
\sim	perturbation quantity
$\hat{}$	unit vector
$\overline{(\)}$	time averaged quantity
$(\)'$	turbulent transport property
$(\)^*$	rate
$*$	reference enthalpy quantity (except δ^*)

Subscripts

bl	boundary layer result
cone	flow quantity on a cone
cp	center of pressure
e	boundary layer edge quantity
F	flow quantity on a flare, or flare location
i	body surface point index
inv	inviscid result
max	maximum
n	nose point on the body surface
r	reference quantity
s	first-order quantity

<i>t</i>	total or stagnation quantity
<i>tr</i>	turbulent quantity
<i>vis</i>	viscous result
<i>w</i>	body surface wall quantity
wedge	flow quantity on a wedge
wind	wind-axis coordinate system
x, y, z	first-derivative with respect to x, y , or z
xx, yy, zz	second-derivative with respect to x, y , or z
σ	based on the body surface distance
∞	freestream quantity

INTENTIONALLY LEFT BLANK.

<u>No of Copies</u>	<u>Organization</u>	<u>No of Copies</u>	<u>Organization</u>
1	Office of the Secretary of Defense OUSD(A) Director, Live Fire Testing ATTN: James F. O'Bryon Washington, DC 20301-3110	1	Director US Army Aviation Research and Technology Activity Ames Research Center Moffett Field, CA 94035-1099
2	Administrator Defense Technical Info Center ATTN: DTIC-DDA Cameron Station Alexandria, VA 22304-6145	1	Commander US Army Missile Command ATTN: AMSMI-RD-CS-R (DOC) Redstone Arsenal, AL 35898-5010
1	HQDA (SARD-TR) WASH DC 20310-0001	1	Commander US Army Tank-Automotive Command ATTN: AMSTA-TSL (Technical Library) Warren, MI 48397-5000
1	Commander US Army Materiel Command ATTN: AMCDRA-ST 5001 Eisenhower Avenue Alexandria, VA 22333-0001	1	Director US Army TRADOC Analysis Command ATTN: ATAA-SL White Sands Missile Range, NM 88002-5502
1	Commander US Army Laboratory Command ATTN: AMSLC-DL Adelphi, MD 20783-1145	(Class. only) 1	Commandant US Army Infantry School ATTN: ATSH-CD (Security Mgr.) Fort Benning, GA 31905-5660
2	Commander US Army, ARDEC ATTN: SMCAR-IMI-I Picatinny Arsenal, NJ 07806-5000	(Unclass. only) 1	Commandant US Army Infantry School ATTN: ATSH-CD-CSO-OR Fort Benning, GA 31905-5660
2	Commander US Army, ARDEC ATTN: SMCAR-TDC Picatinny Arsenal, NJ 07806-5000	1	Air Force Armament Laboratory ATTN: AFATL/DLODL Eglin AFB, FL 32542-5000
1	Director Benet Weapons Laboratory US Army, ARDEC ATTN: SMCAR-CCB-TL Watervliet, NY 12189-4050		<u>Aberdeen Proving Ground</u>
1	Commander US Army Armament, Munitions and Chemical Command ATTN: SMCAR-ESP-L Rock Island, IL 61299-5000	2	Dir, USAMSA ATTN: AMXSY-D AMXSY-MP, H. Cohen
1	Commander US Army Aviation Systems Command ATTN: AMSAV-DACL 4300 Goodfellow Blvd. St. Louis, MO 63120-1798	1	Cdr, USATECOM ATTN: AMSTE-TD
		3	Cdr, CRDEC, AMCCOM ATTN: SMCCR-RSP-A SMCCR-MU SMCCR-MSI
		1	Dir, VLAMO ATTN: AMSLC-VL-D

<u>No. of Copies</u>	<u>Organization</u>	<u>No. of Copies</u>	<u>Organization</u>
1	Commander Naval Surface Warfare Center ATTN: Dr. W. Yanta Aerodynamics Branch K-24, Bldg. 402-12 White Oak Laboratory Silver Spring, MD 20910	1	Rockwell International Science Center ATTN: Dr. S. Chakravarthy 1049 Camino Dos Rios P.O. Box 1085 Thousand Oaks, CA 91360
1	Director Lawrence Livermore National Laboratory ATTN: Mail Code L-35 (Mr. T. Morgan) P.O. Box 808 Livermore, CA 94550	1	Arizona State University Department of Mechanical and Energy Systems Engineering ATTN: G.P. Neitzel Tempe, AZ 85281
1	Director National Aeronautics and Space Administration Langley Research Center ATTN: Technical Library Langley Station Hampton, VA 23365	1	Director Johns Hopkins University Applied Physics Laboratory ATTN: Dr. Fred Billig Johns Hopkins Road Laurel, MD 20707
1	Director National Aeronautics and Space Administration Marshall Space Flight Center ATTN: Dr. W.W. Fowlis Huntsville, AL 35812	1	North Carolina State University Mechanical and Aerospace Engineering Department ATTN: F.F. DeJarnette Raleigh, NC 27607
1	Director Sandia National Laboratories ATTN: Dr. W. Oberkampf Division 1636 Albuquerque, NM 87185	1	Northwestern University Dept. of Engineering Science and Applied Mathematics ATTN: Dr. S.H. Davis Evanston, IL 60201
1	Aerospace Corporation Aero-Engineering Subdivision ATTN: Walter F. Reddall El Segundo, CA 90245	1	Renssalaer Polytechnic Institute Department of Math Sciences Troy, NY 12181
1	Calspan Corporation ATTN: W. Rae P.O. Box 400 Buffalo, NY 14225	2	University of California - Davis ATTN: Dr. Harry A. Dwyer Dr. Joseph Steger Davis, CA 95616
1	Hughes Aircraft ATTN: Dr. John McIntyre Mail Code S41/B323 P.O. Box 92919 Los Angeles, CA 90009	1	University of Maryland ATTN: J.D. Anderson College Park, MD 20740
		1	University of Maryland Baltimore County Department of Mathematics ATTN: Dr. Y.M. Lynn 5401 Wilkens Avenue Baltimore, MD 21228

<u>No. of Copies</u>	<u>Organization</u>
2	Univ. of Southern California Dept. of Aerospace Engineering ATTN: T. Maxworthy P. Weidman Los Angeles, CA 90007
 <u>Aberdeen Proving Ground</u>	
	Director, USAMSAA ATTN: AMXSY-RA, R. Scungio
	Commander, USATECOM ATTN: AMSTE-TE-F, W. Vomocil AMCPM-SMK-M, J. Callahan PM-SMOKE, Bldg. 324
	Commander, CRDEC, AMCCOM ATTN: SMOCR-MU W. Dee C. Hughes F. Dagostin D. Bromley C. Jeffers L. Shaft ATTN: SMCCR-RSP-A M. Miller

USER EVALUATION SHEET/CHANGE OF ADDRESS

This Laboratory undertakes a continuing effort to improve the quality of the reports it publishes. Your comments/answers to the items/questions below will aid us in our efforts.

1. BRL Report Number NR:-TR-3119 Date of Report JUN 90

2. Date Report Received _____

3. Does this report satisfy a need? (Comment on purpose, related project, or other area of interest for which the report will be used.) _____

4. Specifically, how is the report being used? (Information source, design data, procedure, source of ideas, etc.) _____

5. Has the information in this report led to any quantitative savings as far as man-hours or dollars saved, operating costs avoided, or efficiencies achieved, etc? If so, please elaborate. _____

6. General Comments. What do you think should be changed to improve future reports? (Indicate changes to organization, technical content, format, etc.) _____

Name _____

CURRENT ADDRESS Organization _____

Address _____

City, State, Zip Code _____

7. If indicating a Change of Address or Address Correction, please provide the New or Correct Address in Block 6 above and the Old or Incorrect address below.

Name _____

OLD ADDRESS Organization _____

Address _____

City, State, Zip Code _____

(Remove this sheet, fold as indicated, staple or tape closed, and mail.)

-----FOLD HERE-----

DEPARTMENT OF THE ARMY

Director
U.S. Army Ballistic Research Laboratory
ATTN: SLCBR-DD-T
Aberdeen Proving Ground, MD 21005-5066
OFFICIAL BUSINESS

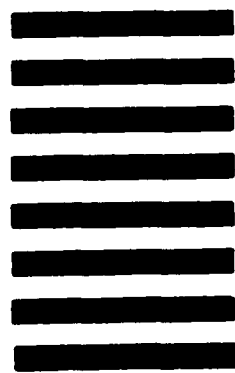


NO POSTAGE
NECESSARY
IF MAILED
IN THE
UNITED STATES

BUSINESS REPLY MAIL
FIRST CLASS PERMIT NO 0001, APG, MD

POSTAGE WILL BE PAID BY ADDRESSEE

Director
U.S. Army Ballistic Research Laboratory
ATTN: SLCBR-DD-T
Aberdeen Proving Ground, MD 21005-9989



-----FOLD HERE-----